TÉCNICO LISBOA

Robot for electrical energy transmission lines inspection

João Pedro Riscado Eanes

Thesis to obtain the Master of Science Degree in

Electrical and Computer Engineering

Supervisor(s): Professor João Sequeira Engenheiro José Moreira

Examination Committee

Chairperson: Prof. João Manuel de Freitas Xavier
Supervisor: Prof. José da Costa Moreira
Member of the Committee: Prof. Sónia Maria Nunes dos Santos Paulo Ferreira Pinto

December 2023

Declaration

I declare that this document is an original work of my own authorship and that it fulfills all the requirements of the Code of Conduct and Good Practices of the Universidade de Lisboa.

Acknowledgments

First of all, I would like to express my gratitude to Professor João Sequeira and Engineer José Moreira for their guidance and support throughout this work.

I would also like to mention the partnership with REN, to which I am very grateful for the opportunity to develop this project.

I would like to thank Engineer Susana Ludovico for her integration and support at the beginning of this partnership, and engineer Raquel Costa for her support during the final phase of the project.

I would also like to thank engineer David Bidarra for his guidance, help and patience throughout the process.

I would like to thank all the workers at the Palmela and Sacavém substations for their constant support and availability during the field tests, as well as for supplying essential material for the sensor tests.

To my colleagues at Istarlabs, for their collaboration in 3D printing the components needed to complete this project.

To my colleague António Neves, thank you for your support during the laboratory tests, which were fundamental to the success of this work.

Finally, a special thanks to my friends and family, especially to my friends André and Madalena, who played a vital role in offering constant help, support and patience throughout the development of this project.

Resumo

Esta tese tem como objetivos a exploração da mobilidade de um robô suspenso em linhas e no desenvolvimento e teste de um protótipo em bancada de laboratório de um sensor para inspeção de linhas aéreas. Os ensaios de mobilidade foram realizados, utilizando um protótipo de teste, numa instalação de testes criada para o efeito na Subestação de Palmela da REN, constitutida por um cabo suspenso por duas estruturas. Os ensaios envolveram a avaliação do movimento do robot, especialmente a sua capacidade de navegar em declives e ultrapassar obstáculos. Embora o robô tenha demonstrado uma boa mobilidade em várias condições, o principal desafio consistiu em ultrapassar obstáculos de forma eficaz. Observou-se, nomeadamente, que o robô conseguia passar por separadores, embora com algumas limitações, especialmente quando não estava numa posição reta e equilibrada. Além disso, foi realizada uma simulação básica de controlo de tração e velocidade, em preparação para futuros testes e implementação, para resolver a questão do deslizamento e da velocidade do robô.

O foco principal desta investigação é o desenvolvimento e teste de um protótipo de sensor em bancada de laboratório. Foi testado um protótipo de sensor de correntes de Foucault, a frequencias entre 8Hz e 80kHz, em várias amostras, aumentando gradualmente a sua complexidade até atingir o nível de um cabo ACSR. Os resultados demonstraram a capacidade do protótipo de bancada de laboratório para detetar tanto cortes superficiais nos fios como corrosão superficial. A deteção foi conseguida através da monitorização das variações da corrente da bobina na presença de defeitos, resultando numa variação aproximada de 10% e em detecções parciais de cerca de 4% provando que este sensor é capaz de detetar cortes com comprimentos entre 1 e 5 cm, bem como entre 2 e 6 fios cortados. Estes resultados provam que este tipo de protótipo é adequado para integração no robô, proporcionando a capacidade de identificar tanto a corrosão como os cortes de fios com um único sensor de correntes de Foucault.

Palavras-chave: Linhas de transmissão aérea, Robô suspenso na linha, ACSR, Correntes de Foucault

Abstract

This thesis focuses on exploring the mobility of a line-suspended robot and the development and testing of a lab bench prototype of a sensor for inspecting overhead lines. The mobility tests were carried out using a test prototype in a test facility created for this purpose at REN's Palmela substation, consisting of a cable suspended from two structures. The trials involved evaluating the robot's movement, especially its ability to navigate slopes and overcome obstacles. While the robot exhibited good mobility under various conditions, the primary challenge lay in effectively overcoming obstacles. Notably, it was observed that the robot could pass through space dampers, albeit with some limitations, especially when it was not in a straight, balanced position. Additionally, a basic traction and speed control simulation was conducted in preparation for future testing and implementation to address the issue of the robot's slip and speed.

The core focus of this research is the development and testing of a lab bench prototype sensor. Was tested in the laboratory an eddy current sensor prototype at frequencies between 8Hz, and 80kHz, across various samples, incrementally increasing in complexity until it reached the level of an ACSR cable. The results showcased the lab bench prototype's ability to detect both superficial cuts in the strands and surface corrosion. Detection was achieved by monitoring variations in the coil's current in the presence of defects, resulting in an approximate variation of 10% and partial detections of around 4% proving that this sensor is capable of detecting cuts with lengths between 1 and 5 cm as well as between 2 and 6 strands cut. These findings prove that this type of sensor is well-suited for integration into the line-suspended robot, providing the capability to identify both corrosion and strand cuts with a single eddy current sensor.

Keywords: Line-Suspended Robot, Overhead line, ACSR, Eddy currents

Contents

List of Tables

List of Figures

Nomenclature

AAAC All Aluminum Alloy Conductor.

AACSR Aluminum Alloy Conductor Steel Reinforced.

ACSR Aluminum Conductor Steel Reinforced.

GNSS Global Navigation Satellite System

HTS High-Temperature Super

LF Localized Fault

LMA Loss of Metallic Area

LWNCI Live-line Working Non-Ceramic Insulator

NDT Non-Destructive Testing

OHL OverHead Line

PEC Pulsed Eddy Currents

PIR Passive Infrared Radiation

SQUID Superconducting Quantum Interference Device

UAV Unmanned Aerial Vehicles

Chapter 1

Introduction

1.1 Motivation

Electricity is an essential part of people's everyday lives. In the last decades of the 19th century, electric power began to be commercially viable. As a result, electric lines were installed in several cities around the world. Electricity is transported by wires attached to a massive network of utility poles [1]. The national electricity transmission network in Portugal consisted of 9,424 km of high-voltage overhead wires as of 2022. These lines usually consist of [2]:

- Towers;
- Cables:
  - Conductors Cables:
    - Insulators;
    - Clamps;
    - Unions;
    - Vibration dampers;
    - Space dampers;
  - Guard Cables:
    - Aircraft Warning Markers;
    - Bird Flight Diverter.

Various types of conductors are frequently employed for transmitting electrical energy, such as All Aluminum Alloy Conductors (AAAC), Aluminum Conductor Steel Reinforced (ACSR), and Aluminum Alloy Conductor Steel Reinforced (AACSR). These conductors are chosen for their robust mechanical and electrical characteristics [3], but they remain vulnerable to damage caused by environmental factors and their inherent fragility [4].

Flashover, an abnormal electrical discharge caused by ionized air, and prolonged wildfires with extreme temperature conditions, can induce birdcaging in the aluminum conductor. Birdcaging happens when aluminum buckles and flares outward radially, creating shapes resembling birdcages. This occurrence can result in an overload of the conductor core and, in certain instances, even lead to the aluminum melting [4].

Pollution can also harm electrical conductors in various ways. For instance, if the conductor's surface is exposed to polluted air containing corrosive chemicals, it can lead to atmospheric corrosion. This type of corrosion weakens the conductor, making it more vulnerable to failure. Another form of pollution-induced damage is the reduction of the dielectric rigidity of the insulation surrounding the conductor. When the insulation is exposed to rain and humidity, it becomes less effective at protecting the conductor from electrical damage. Polluted atmospheres containing water-soluble compounds can create electrically conductive solutions, further increasing the risk of corrosion and damage to the conductor. Such environments are common sources of electrical corrosion in conductors [3].

As noted above, conductors are susceptible and are often subject to corrosion, which often goes undetected even when the degradation is well advanced. Some examples of conductor corrosion include localized pitting, crevice corrosion, galvanic corrosion, and steel corrosion due to galvanization loss.

Aside from environmental factors, other issues can cause damage to electrical cables, such as improper conductor installation or fittings. For example, a gap between the conductor and the fitting can cause wear and abrasion damage to the outer layer of the cable, which can then spread to the inner layers [4].

Early detection of conductor damage is critical because different types of damage can have different consequences. Visual inspection can detect damage in the outer layers, but some damage may be present in the inner layers and not be visible. Regular inspections can detect and repair any problems before they cause major damage or failure [4]. Several methods of visually inspecting conductors include in-person walk-throughs and aerial investigations.

In an in-person walk-through, a group of people follow the line on foot and assess it using their vision, binoculars, or heat sensors. However, this method has several drawbacks, such as being limited by the distance from the conductor, having results that can vary depending on the person performing the inspection, not being able to access certain sites on foot, and being very slow.

In-person aerial assessment involves a helicopter with a crew that inspects and documents the line as the aircraft travels along it. This method is faster and more accurate, but it still relies on the worker performing the inspection, poses risks due to the helicopter flying close to the line, and can be costly [3].

In addition to in-person inspection, helicopters can also be used for automated inspection using infrared sensors that can detect hotspots, which can indicate corrosion on the conductor or a junction that needs to be repaired or closely monitored. This method provides data that can help to determine the severity of the conductor damage [3]. The labeling system for hotspots is shown in Table 1.1.

Table 1.1: Classification of conductor damage [4]

Maintenance Condition Rating	Observation:	Action
A	Like new	No action
B	Minor defect: low number of repairable broken wires ($\geq 25\%$), flash burns	Install repair rods
C	Moderate defect: Bird caging, mild evidence of corrosion, high number of repairable broken wires ($\geq 50\%$)	Consult engineering, Install repair rods
D	Serious defect: Severe damage to multiple wires ($\geq 75\%$), unraveling/core exposed, significant evidence of corrosion.	Repair/Replace

On the Overhead Lines (OHL), maintenance depends not only on the nature and severity of the damage but also on its location. The consequences of damage can vary significantly depending on the line and the section where the cable experiences a breakage. In some cases, this can lead to a substantial power loss for a large section of the population, and there's also the risk of accidents involving vehicles and individuals if the cable falls. Therefore, in placement analysis, three crucial factors must be taken into account: the location of the damaged conductor section (e.g., river crossing, road crossing), the number of repairs needed within the section, and the distance between fittings within the span [4]. The various repair criteria are detailed in Table 1.2.

Table 1.2: Criteria for different repair methods [4]

Respondent ID	Criteria	Action
A	Presence of more than three repair fittings within a single span	Consult engineering for evaluation of reconductoring options
B	Presence of "several" Hyper-Converged Infrastructure (HCI) repair fittings within a line	Remove and replace conductor for the whole line section
C	Presence of more than three repair fittings per kilometer	Remove and replace conductor

As discussed in this section, it is of utmost importance to maintain a continuously operational electrical power transmission system, which necessitates meticulous planning and ongoing monitoring. However, the techniques employed for line maintenance often involve human workers ascending the lines to repair or replace fittings. This work can be hazardous due to the high voltages carried by the lines and the elevated working conditions. Additionally, the use of helicopters for line inspections is costly and poses potential risks due to crew errors, weather conditions, or equipment malfunctions. These risks underscore the significance of prioritizing the safety of both workers and the general public during overhead line maintenance and inspection [1].

According to the Bureau of Labor Statistics, power line installers and repairers consistently ranked among the most perilous occupations from 2011 to 2015, with higher nonfatal injury rates compared to workers in other professions. Table 1.3 provides data on the number of injuries each year within the period. There were 131 fatal injuries over those years, with minimal year-to-year variation in the fatality count. Table 1.4 illustrates the number of days absent from work following an injury. The considerable number of days away from work, with an average of 8 days per injury, suggests that electrical line repairers and installers frequently experience severe injuries [1].

Table 1.3: Number of work injuries of electrical power-line workers in America [1]

Year	Fatal injuries	Non fatal injuries
2011	26	2500
2012	27	2090
2013	27	2310
2014	25	2510
2015	26	2240

Earlier, we underscored the significance of detecting defects in specific areas of the power line. However, current inspection methods are confined to assessing the outer layers of the conductor, which often compels the utility provider to adhere to the practice of replacing conductors solely based on

Table 1.4: Distribution of nonfatal occupational injuries and illnesses by the days away from work [1]

Days away from work	Electrical power-line installers and repairers (%)
3-5	21.0
6-10	6.6
11-20	10.8
21-30	6.0
31 or more	44.3

their installation date. This approach results in the frequent replacement of conductors in good condition situated in less challenging environments. More critically, it leaves newer conductors, which have already been compromised by the harsh environment, in active service.

1.2 Topic Overview

Ensuring the safety of line workers and the general public is of utmost importance, and the use of robots for the inspection and repair of electrical cables can be an effective approach to achieve this objective. In addition to enhancing safety, employing robots in overhead line maintenance can lead to improved efficiency, access to previously inaccessible areas, and cost reduction. A variety of robot types are currently in use for overhead line maintenance and inspection, as described in [5]. Some of the robot types employed include:

- Line Suspended Robots;
- Unmanned Aerial Vehicles (UAV);
- Ground Based Robots;
- Other Types of Robots (e.g. climbing robots and insulator robots).

Line Suspended Robots are specifically designed to act as an extension of transmission linemen's capabilities. These robots can traverse transmission lines and surmount obstacles. The incorporation of robots in line inspection streamlines the assessment of steel core wire conditions, detection of broken wires, measurement of remaining cross-sections, and, at times, even temporary component repairs. This enhances inspection accuracy, simplifies access to hard-to-reach spans, and reduces risks for linemen [5].

As an alternative to helicopters, Unmanned Aerial Vehicles (UAVs) can be employed for in-line inspection of power lines. These autonomous robots can safely navigate in close proximity to the lines and transmit images wirelessly to ground-based workers. This eliminates the need for a human operator to be physically present near the lines, significantly improving safety and efficiency [5].

Ground-based robots are under development to capture and control electrified conductors, enabling them to perform tasks beyond human capabilities, such as repairing and replacing structures or insulators. These technologies focus on the development of robotic arms for manipulation and control of electrified conductors [5].

Despite advancements in robotic technology, certain critical components of overhead line infrastructure remain inaccessible for inspection by robots in the aforementioned categories. This includes

insulators, towers, and jumpers. Various other types of robots are being developed to address these challenges, including tower and pole climbing robots and insulator inspection and cleaning robots [5].

Chapter 2 will provide an overview of current and in-development robots for line inspection and maintenance, along with relevant use cases and examples.

1.3 Objective

Overall, the objective of this study is to assess the practicality and effectiveness of using a line-suspended robot for inspecting energy transmission lines. The objectives of the prototype can be categorized into three distinct areas:

- Locomotion;
- Damage detection;
- Data analysis.

The first objective of this study is to design and contribute to the development of a prototype for a line-suspended robot that can be used to inspect energy transmission lines. It is intended to evaluate the prototype's ability to move along the lines.

The robot must operate on electrified lines, including simple cables with diameters ranging from 14.60 mm to 31.8 mm, and it should be capable of traveling over a span of 500 meters with a maximum slope of 40 m when manually linked to the line. While these objectives pertain to lines without obstacles, the ability to overcome some obstacles will be studied as a secondary objective.

The second objective of this study is to design and test a sensor that can be attached to the robot in order to detect flaws in the conductor.

The robot's sensor must be able to identify broken wires inside the cables, detect internal corrosion, assess section loss in the internal wires, and determine zinc thickness loss in the internal steel wires to meet the inspection objectives.

Finally, if possible, the development of software to process the sensor data and control the movement of the robot.

After achieving an operational robot capable of traversing the line and conducting inspections, the ultimate goal is to create software that can assess data collected by sensors in real-time and generate a report categorizing existing damage in terms of intervention urgency.

1.4 Planned Mode of operation

To comprehend the requirements for achieving the objectives, it was imperative to outline the operation of the robot. Given that the primary goal of the robot is to traverse a straight path, the focus is primarily on velocity, traction control, and data handling. The operational details of the robot are illustrated in Figure 1.1.

The first pool encompasses all the functions performed from the ground. It commences with the initial setup, where each operator initiates the control software and establishes connections between the two

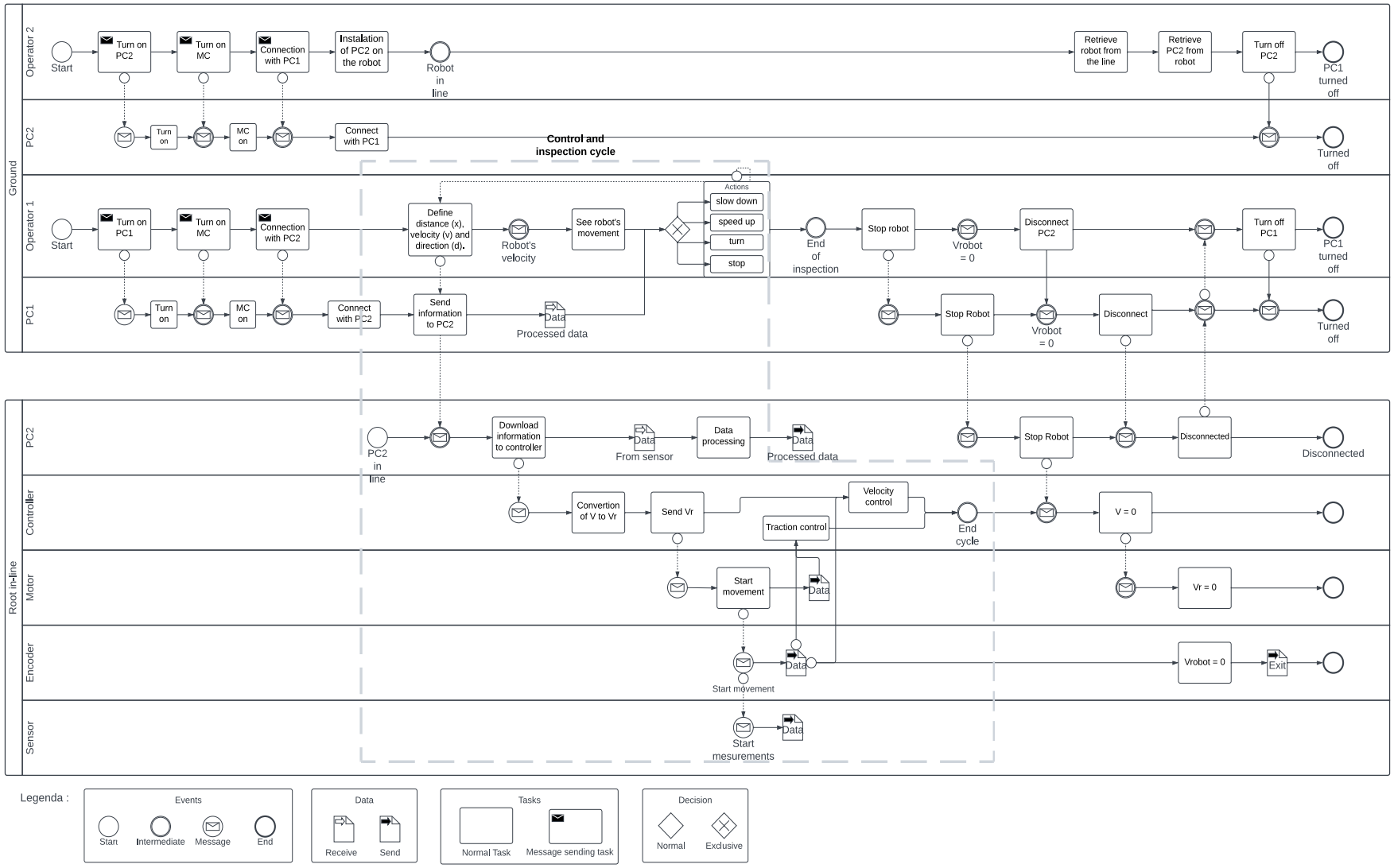

Figure 1.1: Robot's mode of operation

PCs. Following initialization, PC2 is affixed to the robot, which is then hoisted by an operator to attach it to the line. As depicted in the same pool above, the ground operator initiates the robot's movement by selecting parameters such as speed, the distance to be inspected, and the direction. Throughout the inspection, the operator can control the robot's movement by adjusting speed and direction. Upon completing the inspection, the robot is brought to a halt, the PCs are disconnected, and the robot is retrieved from the line.

The second pool outlines the robot's operation on the line, where it receives instructions from PC2 and acts upon them. In this process, the encoder and motors continually transmit data about the rotation speed to PC2 for computing speed and traction control. This cycle persists until PC2 receives the signal to conclude the movement. Simultaneously, the sensor transmits collected data to PC2 for processing and real-time transmission to the ground-based PC. This enables the operator to analyze graphical data, identify defects, and, if necessary, instruct the robot to pass through a span where the sensor's response is not 100% clear.

The details of the speed and traction control, as represented in Figure 1.1, are provided in greater depth in Figure 1.2.

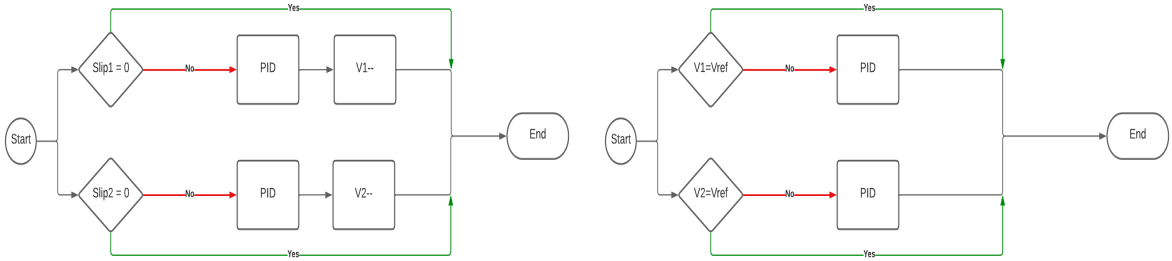

(a) (b)

Figure 1.2: Control of the robot: (a) Speed control; (b) Traction control.

Regarding speed control, the rationale is to allow the sensor sufficient time to collect ample data for precise defect detection. Hence, the velocity should remain slow and consistent throughout the entire trajectory. Since the robot's obstacle-passing capability relies solely on the wheel design, it's essential that the standard velocity is set high enough to overcome obstacles but not so high that it compromises the robot's stability. Once the ideal velocity is determined, the next step is to implement a control mechanism that can maintain this velocity. This can be achieved with a straightforward PI/PID controller, as each wheel is directly connected to a motor. Synchronization of both wheels is essential to ensure the robot's speed remains constant.

Traction control involves keeping slip at approximately zero, and for this purpose, slip must be continually calculated. It's important to note that traction control is only necessary when there is slip. In cases where the speed of the traction wheels matches that of the support wheels, representing the robot's overall speed, the control remains inactive and is reactivated when required. Similar to the velocity control, the PID controller is employed to approximate the slip value to its ideal value.

1.5 Thesis Outline

In this thesis, a structured approach is adopted, commencing with Chapter 1, ”Introduction.” This chapter provides a comprehensive overview of the project’s context, and presents the problem to be addressed.

Chapter 2, ”Background,” is dedicated to enhancing the comprehension of the project’s context by exploring existing technologies and identifying areas where this project can make a meaningful contribution. This chapter also introduces the theoretical framework that serves as a guiding foundation for the work at hand.

Proceeding to Chapter 3, titled ”Implementation,” this section provides a comprehensive description of the methods and trials employed to advance the project and achieve its objectives. It offers an account of the practical steps taken during the project’s development.

Chapter 4, ”Results,” is the section where all the findings obtained throughout the work are presented, analyzed, and compared with the existing literature, and where the implications of these results are explored.

Chapter 5, the ”Conclusion,” summarizes key findings, emphasizes the contributions of our study, acknowledges limitations, and suggests avenues for future research.

Chapter 2

Background

The use of robots in overhead power line inspection has witnessed substantial growth since the 1990s, and this trend has accelerated in the 2000s. Presently, a diverse range of robots with various applications for in-line inspection is available [5]. These robotic systems, designed to assist linemen in inspecting and maintaining power lines, contribute to enhancing the reliability and safety of the electrical grid. Additionally, these systems reduce maintenance and repair durations and grant access to challenging-to-reach line segments. While the primary focus of most overhead line robots is inspection, some of these systems are also equipped to perform certain maintenance tasks [5].

- **Line Inspection :**

  Traditionally, power line inspections were conducted by ground crews and helicopters. However, in recent years, robots have become indispensable for these tasks. Robots excel in various roles related to visualization and inspection, which include evaluating the condition and pinpointing the locations of towers and their foundations, scrutinizing cables, fittings, and insulators for potential issues, and mapping the route of the power line. Among the categories of robots, line-suspended robots and Unmanned Aerial Vehicles (UAVs) offer distinct advantages. Unlike ground-based robots, these aerial systems can be equipped with a diverse array of sensors tailored to the specific inspection requirements. Depending on the sensors integrated into the robot, it can perform tasks such as infrared and ultraviolet inspections, laser-based assessments, and a wide range of measurements, including electrical resistance, current levels, corrosion assessment, corona inspection, conductor temperature monitoring, and even audible noise analysis. These capabilities significantly enhance the precision and comprehensiveness of power line inspections.

- **Line Maintenance :**

  The role of robots in the maintenance of electrical power lines is rapidly expanding, with the belief that this technology may eventually replace human workers in tasks related to overhead power lines. To effectively fulfill these functions, robots must possess the capability to utilize sensor feedback and integrate autonomous subsystems. Currently, robots have demonstrated their proficiency in a wide range of tasks, including replacing ground wires on power lines, removing ice from

conductors, cleaning insulators, replacing damaged insulators, installing aircraft warning spheres, attaching conductor repair clamps and patch bars, substituting energized conductors, repairing or replacing damaged structures, installing and retrieving bolted assemblies, and inspecting and correcting damper positions. This increasing spectrum of tasks performed by robots holds the promise of enhancing the efficiency, safety, and precision of power line maintenance.

Inspection and maintenance are pivotal and high-value activities in power line operations. The potential to perform maintenance while the line is energized, with potential robotic support, offers numerous advantages across environmental, economic, and social dimensions for network owners.

The following sections delve into the domain of contemporary robots, sensors, and inspection methodologies used in power line maintenance. This comprehensive exploration will cover not only line-mounted robots but also all categories of robots, providing insights into both the capabilities and limitations of this technology.

2.1 Line suspended robots

LineScout, Hydro-Québec (Canada)

The LineScout robot, demonstrates an impressive ability to traverse various elements of power lines, including ground wires, individual or bundled conductors, and obstacles up to a height of 0.76 meters. This versatile robot features a directional camera at one end, while the other end can be equipped with tools to facilitate inspections and even perform temporary repairs. These repair tasks include activities such as adjusting and securing bolted assemblies and repairing damaged conductor strands [6].

Notably, LineScout incorporates a clever mechanism that allows it to extend its body to twice its original length, enabling it to effectively overcome obstacles. It accomplishes this by gripping one side of the obstacle with its wheels and then dragging its body to the other side. To execute this intricate maneuver, LineScout consists of three distinct frames: a wheel frame that supports the wheels, a gripper frame equipped with grippers to stabilize the robot as the wheels traverse obstacles, and a floating center responsible for housing the robot's battery, electronics cabinet, and communication systems [6].

Figure 2.1: LineScout [6]

LineVue^{TM}, Kinectrics Inc (Canada)

The LineVue robot is purpose-built for operations involving single conductors with diameters ranging from 15 to 45mm. This remotely operated robotic system utilizes radio communication to transmit essential information to the operator. It is equipped with a camera for real-time assessment of the aluminum conductor's condition, a sensor head dedicated to data collection and measurements, and a tugging mechanism that allows it to travel along the conductor line.

The sensor data is collected, processed, and then presented to the operator in a graphical format. This visual representation provides an evaluation of defect severity along the conductor line, with defects categorized using a color-coded scale. In this scale, red and yellow zones highlight areas requiring immediate and semi-urgent maintenance, respectively, while green areas indicate sections with no significant defects present in the conductor line [5].

Expliner, HiBot (Japan)

Expliner is a semi-automatic robot designed for the simultaneous inspection of multiple electrical conductors. It utilizes a combination of sensors and cameras to capture images of the conductors and measure the diameter of the outer conductor layer, enabling the detection of corrosion in the inner layer. In addition to its inspection capabilities, Expliner is equipped to capture detailed images of various components, including spacers and jumpers.

The robot's structure consists of a T-shaped body with four V-groove traction wheels at the top and a two-degree-of-freedom carbon pipe manipulator at the bottom. This design provides the operator with the ability to control the robot's center of gravity and lift each support point individually. This feature facilitates maneuvering the robot around obstacles, as demonstrated in figure 2.2 [7].

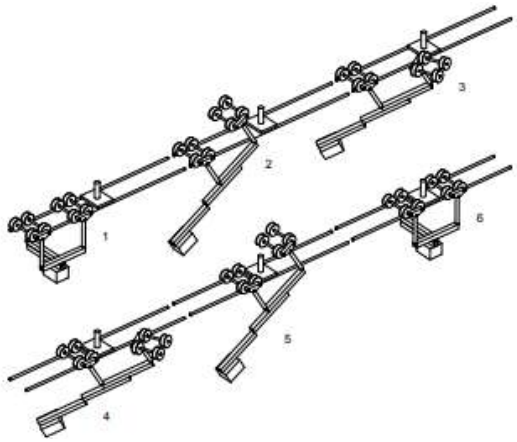

Figure 2.2: Expliner's method to surpass suspension clamps [7]

AApe-D, Chinese Academy of Sciences (China)

The Chinese Academy of Sciences has developed various iterations of AApe robots, with the latest version being the AApe-D. This ground-operated robot is engineered to navigate obstacles and access areas where damaged strands require repair. It is equipped with two essential tools: the looper and

the clamper. The looper is used to restore broken strands to their original position on the conductor, while the clamper is employed to repair damaged sections by installing a specialized clamp to prevent strand unwinding. The primary goal of this robot is to ensure mechanical strength and conductivity, thus reducing the necessity for manual maintenance following a power outage [8].

Power Line Inspection Robot (PLIR), University of KwaZulu-Natal and Eskom (South Africa), Transpower (New Zealand)

The Power Line Inspection Robot (PLIR) shares common obstacle avoidance features with other inspection robots. However, its distinctive feature lies in its capability to traverse along jumper wires. This unique ability enables it to access challenging or remote areas and conduct comprehensive power line inspections, setting it apart from previous robot models [5]. The procedure for transitioning to a jumper wire is illustrated in Figure 2.3.

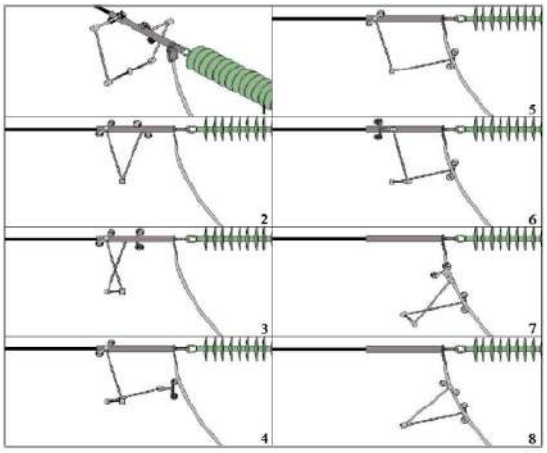

Figure 2.3: PLIR's method to switch to the jumper lines [5]

Transmission Line Inspection Robot (Ti), EPRI (USA)

The Ti robot, designed for continuous operation on transmission lines, operates autonomously and is equipped with sensors and cameras to detect broken components and areas in need of vegetation trimming. The robot comprises two ”trucks,” each equipped with rollers and a motorized wheel to grasp the shield wire. To overcome obstacles, the Ti robot relies on the construction of bypass devices installed on the components it must traverse. When the Ti detects a bypass system, it navigates around obstacles using a method similar to that of the LineScout. When it encounters an obstacle, it releases its ”trucks” and sequentially moves them to the other side of the obstacle, ensuring uninterrupted inspection without hindrance [5].

The robot is provided with a predefined protocol to specify the type of inspection required and the number of components to be inspected. While the Ti robot can generate a comprehensive report, its primary focus is on reporting anomalies. Additionally, the Ti robot is equipped with a built-in mechanical arm for inserting a grounded plate into the line, facilitating battery recharging. In emergency situations, it can also utilize integrated solar panels as an alternative power source [5].

Conductor Corrosion Assessment System (CCAS), Shannon Technology (Canada)

The CCAS robot is specially designed to analyze the zinc content in the galvanized steel core wires within ACSR conductors. This robot conducts its analysis by collecting data at regular intervals along the line, covering approximately 10% of the entire circuit's length. The evaluation process involves assessing each span individually and classifying it using a four-number system, as detailed in Table 2.1. These individual span profiles are then aggregated to provide a comprehensive assessment of the entire circuit [5].

Table 2.1: CCAS classification system [5]

Grade	Description	Remaining zinc
1	No loss	Practically new
2	Minimal loss	50% or more
3	Partial loss	20% to 50%
4	Full loss	0% to 20%

Traction Machine

The Traction Machine is a remotely controlled device powered by two electric motors and a battery. It is purpose-built for the replacement of ground wires and is equipped with two large traction wheels and four smaller support wheels. When elevated to the cable level, it securely holds its position by applying pressure on the cable between the traction and support wheels. The robot's battery box is strategically designed to maintain balance, and it can surmount obstacles up to 60mm in height, thanks to the V-shaped grooves on its wheels [9].

Figure 2.4: Traction Machine [9]

2.2 Unmanned Air Vehicles (UAV)

Electric power companies are increasingly investing in the development of Unmanned Aerial Vehicles (UAVs) for power line inspections. These UAVs provide clear images and unique inspection perspectives when flying in close proximity to tension lines. This technological advancement allows for a reduction in the frequency of helicopter inspections [10]. While the development of UAVs for this application is still in its early stages, today's UAVs are primarily utilized for military purposes.

These robots have the capability to track their own positions, enabling autonomous behavior. In the context of power lines, they are primarily employed for tasks such as monitoring high-risk vegetation encroachment, inspecting power line corridors, and conducting visual inspections using various camera systems. The technology is expected to gain wider adoption as more competitors enter the market. However, there are challenges associated with UAVs, including the risk of equipment malfunctions, potential privacy concerns, compliance with regulations imposed by aviation authorities, and unpredictable environmental factors such as wind gusts.

This section will specifically focus on the various types of UAVs used in power transmission line inspections, given the numerous UAV models available [5].

Fixed-Wing Aircraft

The majority of commercially available UAVs for power line inspections are fixed-wing aircraft. These robots are characterized by a main wing, one or two tail wings, and a motor positioned behind the main wing or at the rear of the aircraft. This design enhances stability in crosswinds and provides better control at high operating speeds [5].

Fixed-wing UAVs have the capability to operate at a wide range of speeds, with a minimum cruise speed of 10 m/s, and sometimes even lower with extremely light payloads. However, a drawback of this type of UAV is its limited ability to capture high-precision images of power lines due to its high speed. On the other hand, fixed-wing aircraft excel at flying in adverse weather conditions and quickly reaching remote and challenging-to-access locations [5]. Various types of winged-fixed aircraft are illustrated in figure 2.5.

Figure 2.5: Example of Winged-Fixed Aircraft [10]

Helicopter

When a higher payload capacity is required, helicopters are employed for power line maintenance. These mechanical devices typically feature two rotors, a larger main rotor, and a smaller secondary rotor at the tail, although their size and placement can vary. Helicopters are equipped with various mechanical systems, as outlined in references [5, 11]:

- A flight control system that allows autonomous navigation;
- A communication system that allows control of the helicopter by ground operators and transmission of information to the helicopter via telemetry;
- An image stabilization system, eliminating vibrations and providing high-resolution images;
- Can be equipped with a gyro-stabilized camera and high optical zoom system for high-speed operation.

Safety is of paramount importance when operating unmanned helicopters for power line maintenance. These robots can weigh up to 100 kg and carry up to 20 kg of highly flammable fuel. Consequently, it is not recommended to use the fully autonomous mode in areas with a high population density or near industrial areas.

The flight control system of these helicopters incorporates an Inertial Navigation System and a Differential Global Positioning System. A microprocessor uses data from these sensors to provide autonomous navigation control by following predetermined ”waypoints.” Additionally, a navigation module can detect magnetic fields and enable safe navigation when the strength of a particular field exceeds a certain threshold. These safety measures are crucial to ensure responsible and secure operations in power line inspection, as mentioned in reference [5].

Figure 2.6: Example of Unmanned Helicopter [11]

Multicopter

Multicopters are versatile aerial vehicles with three or more rotors, controlled by adjusting rotor speeds. They offer agility and ease of control in various directions, making them a promising technology for power line inspection. Equipped with lightweight batteries, advanced sensors, and efficient motors, multicopters are gaining prominence in this field.

These robots rely on gyroscopes, magnetometers, and acceleration sensors for stability and hover control. They come in different sizes, typically ranging from 0.5 to 1.5 meters, with the choice depending

on payload and maneuverability requirements. For safety, it is advisable to use multicopters with five or more rotors to account for potential rotor failure. They can be remotely piloted or feature GNSS navigation controls, with advanced models incorporating LIDAR for 3D mapping, collision avoidance, and autonomous takeoff and landing.

State-of-the-art multicopters offer flight durations of 20-60 minutes, capable of carrying payloads ranging from 0.5 to 3 kilograms, and operating at speeds between 3 and 10 m/s over ranges of 4-35 km. Design considerations for multicopters include safeguarding sensitive components like antennas and sensors [5].

Multicopters find significant use in visual inspections, capturing images of components or structures during power line inspections. These images can be analyzed in real-time or later to identify potential problem areas or concerns that require attention [5]. An example of a multicopter is shown in Figure 2.7.

Figure 2.7: Example of a Hexacopter [5]

2.3 Ground-Based Robots

Ground-based robots employed in the power transmission and distribution sector primarily focus on improving safety by enabling the secure management of energized conductors and creating safer working conditions for linemen. A significant portion of the research and development efforts in this field are dedicated to the design of robotic arms, specifically crafted for manipulating and controlling energized conductors [5].

Three Phase and Single Pick Robotic Arm

The LineMaster^{TM}, developed by Quanta Service, is a ground-based robot equipped with a three-phase picking arm, and it is currently utilized for electrical tasks worldwide [12]. This robotic arm is remotely operated through a control system comprising a portable transmitter and two receivers. It is powered by hydraulic pressure, which can be supplied from either a remote hydraulic source or directly from the hydraulic tool ports of a truck or aerial lift. The arm was specifically designed for the challenging tasks of re-framing and re-insulating buildings that are typically difficult to work on with standard equipment. Additionally, it can replace old or damaged poles, making use of existing holes [12].

In addition to the LineMaster^{TM}, there is the Single Select Robotic Arm, designed for the remote selection and operation of one phase at a time. This arm is engineered to handle larger conductor diameters and heavier weights. It can be employed for urgent conductor repairs and support when a

replacement structure is not yet available. With the line energized, the arm can be adjusted to fit the structure's frame, securely grip the conductor, and safely move it away from the structure for removal or re-framing.

Phase Lifter

The LineWise Hydraulic Phase Lifter is a ground-based robot designed for energized work. It features an insulated crane capable of supporting three phases and is versatile enough for both horizontal and vertical applications. The Phase Lifter boasts a maximum lifting capacity of 680.4 kilograms in the vertical position and 102.1 kilograms in the horizontal position.

Constructed with fiberglass arms, the robot can be equipped with standard insulators or sealed fiberglass insulators, which can be easily attached to the Phase Lifter without the need for any tools. Additionally, it is highly adjustable, with adapter links that allow the Phase Lifter to be set at various angles to the floor. For reference, figure 2.8 provides an image of a LineWise Phase Lifter [5].

Figure 2.8: LineWise Phase Lifter

Robotic Pole Manipulator

This robotic system is engineered for the replacement of power poles within the length range of 12.2 to 16.8 meters. It encompasses a truck-mounted crane equipped with a hydraulic gripper designed to manipulate the poles. This innovation holds significant importance due to the substantial number of aging power poles within electrical grids [5].

2.4 Other types of robot

Despite the advancements in electrical energy transmission lines, certain components of overhead power lines, including insulators, towers, and jumper lines, present challenges for inspection and repair using both ground and aerial robots. Previous research has suggested that it is more practical to develop specialized robots tailored for these specific tasks, rather than attempting to create general-purpose robots [5].

Climbing robots

Carnegie Mellon University's snake robot, depicted in figure 2.9(a), serves as an example of a robot that employs snake-like locomotion to climb poles and trees. The Electric Power Research Institute (EPRI) has also demonstrated a snake robot capable of pole climbing and traversing insulator discs. While these robots hold promise for tasks like insulator inspection, their widespread use is hindered by their high cost [5].

International Climbing Machines has developed untethered robots that utilize a vacuum mechanism to ascend metallic and non-metallic towers, as illustrated in figure 2.9(b). These robots are primarily employed for wind turbine maintenance [5].

(a) (b)

Figure 2.9: Examples of climbing robots: (a) CMU's snake robot; (b) International Climbing Machines' untethered climbing robot [13].

Insulator robots

The Korea Electric Power Research Institute developed a field robot for live-line insulator inspection following the introduction of the Insulator Washer-I in 1995. Utilizing similar technology, they also created a robot for live-line inspection of suspension insulator strings. This robot can monitor insulation resistance and voltage distribution along the insulator [5].

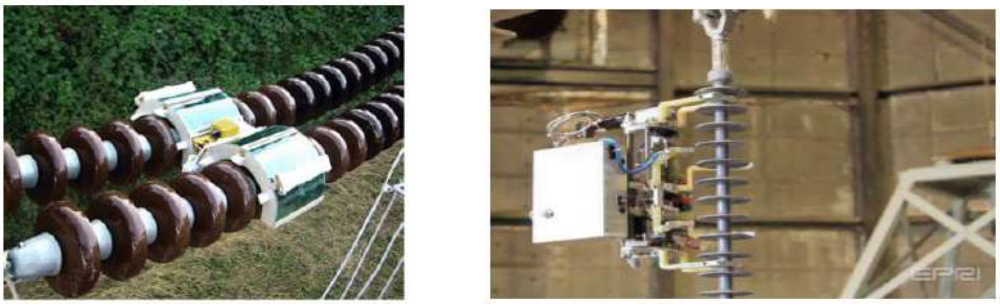

(a) Insulator cleaning robot [5] (b) Robot with LWNCI tool as payload [5]

Figure 2.10: Example of insulator robots

The Electric Power Research Institute (EPRI) has engineered a robot to replace the Live-line Working Non-Ceramic Insulator (LWNCI) tool used for insulator testing. The LWNCI assesses the resonance and capacitance response of ceramic insulators by applying high-frequency and voltage to a 300mm section

of the insulator. EPRI designed an insulator crawler robot capable of carrying the LWNCI tool as a payload and functioning in electrified environments to enhance measurement reproducibility and safety while reducing the mechanical stress on field workers. This robot is intended to navigate insulator strings and conduct measurements more efficiently and safely [5].

This study has unveiled that each type of robot fulfills specific roles. However, when aligning the inspection objectives with the information presented in this chapter, it becomes evident that the most favorable options are line-suspended robots and UAVs. A comparative analysis between the two reveals that line-suspended robots offer several advantages, including close proximity to the conductor, safety, ease of operation, and cost-effectiveness.

The close proximity to the conductor allows for the utilization and adaptation of sensors known for their effectiveness in inspecting both the conductor's surface and interior, as discussed in the sensors section. Furthermore, the fact that these robots move along the conductor eliminates the risk of collision with the line and mitigates the impact of wind, a challenge that UAVs often encounter.

2.5 Sensors

Power line cables are subjected to harsh and prolonged climatic conditions, as discussed in section 1.1. These conditions include factors such as wind, rain, and pollution. If left unaddressed, this exposure can lead to the gradual deterioration of the conductor, resulting in unexpected issues and a decline in the quality of power supply. The consequences of such failures can be severe, potentially affecting a significant portion of the population, causing power outages, and posing risks to vehicles and people, especially if the cable falls onto a highway or in a populated area [14].

Typically, electrical energy lines utilize ASCR conductor cables, as detailed in section 1.1. These cables consist of a steel core that provides mechanical support, while aluminum strands carry the electrical current [15]. The most common defects, such as burns and strand breaks, occur on the outer aluminum layer and can be detected through visual inspection. However, internal defects, particularly those within the steel core, are more challenging as they remain concealed and can reduce the mechanical strength of the conductor, ultimately leading to failure. There are two types of internal steel defects [16]:

- Localized Faults, LF: Consists mainly of broken steel strands.
- Loss of Metallic Area, LMA: Corresponds to a reduction in steel cross-section, often caused by internal corrosion.

Galvanic corrosion in the steel core of ACSR conductors is a well-documented issue, and protective measures are implemented to shield steel conductors. However, significant corrosion can still occur due to various atmospheric factors, including airborne industrial pollutants or exposure to sea salt [17]. In cases where moisture infiltrates the cable's core, particularly when the grease layer is insufficient, the galvanized steel layer initially provides some protection. However, as the steel is exposed, the aluminum becomes anodic and vulnerable to galvanic corrosion. This corrosion process detrimentally impacts both the electrical and mechanical properties of the cable, ultimately leading to cable failure [18].

The most severe corrosion typically occurs on the inner conductors and is challenging to detect visually in its early stages. This section delves into an examination of various techniques commonly employed in overhead power line inspections and explores the sensor considered most suitable for this application.

2.5.1 Sensor Analysis

Non-destructive testing (NDT) stands as a pivotal technique in materials science, employed for the inspection of objects without inducing any damage. Within the realm of electrical engineering, NDT assumes a critical role in the detection, characterization, localization, and sizing of diverse types of discontinuities and faults [17].

While visual inspection has traditionally served as the predominant method for fault detection in power lines, several non-destructive testing (NDT) techniques have been introduced to enhance the precision and localization of such fault detection. These techniques encompass visual inspection, infrared camera inspection, ultrasonic inspection, neutron radiography, magnetic methods, electromagnetic induction (eddy current), and time domain reflectometry [17].

The exploration of passive infrared radiation (PIR) as a means to inspect damaged power lines is notable. This method relies on disparities in dissipation capability and infrared radiation between impaired and intact sections of active conductors. However, it's crucial to note that this approach is sensitive to ambient temperature variations, rendering it susceptible to both missed detections and false alarms [14].

Some researchers have proposed the utilization of ultrasonic waves to inspect power transmission lines for damage. An ultrasonic transducer generates ultrasonic waves within the cable, and in the presence of defects, these waves may undergo partial reflection by the transducer. However, it's important to acknowledge that ultrasonic transducers based on piezoelectric ceramics necessitate an ultrasonic coupler, which can potentially limit portability [14].

Among the array of NDT techniques, electromagnetic methods founded on eddy current induction emerge as one of the most promising approaches for inspecting power lines. Detectors operating on this principle can discern flaws, such as cracks, pits, and reductions in cross-sectional area, at an earlier stage compared to other non-destructive methods. This technique additionally facilitates the quantitative evaluation of the zinc layer thickness, which contributes to the assessment of conductor conditions. Furthermore, these detectors are adaptable to cables of various sizes, including live cables with voltages of up to 500kV [14, 17].

Eddy current inspection technology exhibits a high level of sensitivity, practicality, and relative ease of use when compared to other available methods. It necessitates minimal surface preparation and is capable of penetrating non-conductive coatings, even up to approximately 100 mm in thickness, although its inspection capability decreases at such distances. Nonetheless, it's imperative to recognize certain limitations, such as its applicability exclusively to electrically conductive materials, the requirement for expertise in interpreting complex signals displayed by impedance-plane instruments, and its sensitivity

to alterations in material properties and variations in lift-off, which can occasionally lead to the obscuring of the signal of interest by noise [17].

It is noteworthy that, while eddy current inspection has demonstrated effectiveness in detecting broken steel strands in transmission lines, there have been limitations reported in its ability to detect broken aluminum strands.

Additionally, researchers have explored the utilization of superconducting quantum interference devices (SQUIDs) employing high-temperature superconductors for the detection of breaks in individual wires within transmission lines. This technology has demonstrated the capability to detect periodic distribution patterns along the path of a broken conductor, thereby distinguishing it from normal conductors. Nevertheless, it's essential to recognize that HTS-SQUID systems tend to be large and heavy, which may limit their extensive application in operational conditions [14].

A summary detailing the various sensors employed in power line inspection is provided in table 2.2.

Table 2.2: Study of the sensors

Technique	Sensitivity	Ease of use	Applicable
Visual inspection	2	2	2
Infrared inspection	2	3	2
Ultrasonic inspection	2	3	3
Magnetic flaw detection	1	3	3
Electromagnetic Induction	1	1	1
Legend	Excellent: 1	Fair: 2	Poor: 3

2.5.2 Eddy current sensor

Eddy current sensors have garnered significant attention across various industries owing to their non-contact nature and exceptional sensing precision. These sensors operate on electromagnetic principles to detect alterations in electrical conductivity, offering valuable insights into material characteristics, structural integrity, and precise positioning.

The following sections aim to provide a comprehensive understanding of eddy current sensors commencing by delving into their fundamental principles, encompassing the physics underlying eddy current generation and its interactions with conductive materials, forming the foundational basis for their functionality. Subsequently, it will be explored the primary sensor structures employed for this purpose, address challenges and potential solutions regarding their integration into robotic systems, and conclude by examining various methods for analyzing the experimental results.

2.5.2.1 Fundamental principals

Eddy current sensors operate on the fundamental electromagnetic principle of eddy currents. When a conductive material is subjected to a dynamic magnetic field, it induces circulating currents, known as eddy currents, within the material. These eddy currents, in accordance with Lenz's law, create their own magnetic fields opposing the changes in the applied magnetic field. This interaction leads to a back electromotive force (EMF) in the coil, resulting in an alteration in the coil's impedance. If there is

a surface flaw on the material beneath the coil, it impedes the flow of eddy currents, diminishing the coil's loading and elevating its impedance [19, 20]. Detecting these impedance changes caused by eddy currents relies on several factors:

- **Distance between the coil and the material**: The varying distance between the circuits alters their mutual inductance, leading to a decrease in the amplitude of the eddy currents. This can potentially lead to the misinterpretation of signals as flaws [20].

- **Surface and subsurface geometry**: The shape and size of the conductor have a significant impact on the distribution and magnitude of eddy currents. Typically, thicker and wider conductors will exhibit larger eddy currents, whereas thinner and narrower ones will have smaller eddy currents [20].

- **The conductivity of the material**: Materials characterized by increased conductivity, such as copper and aluminum, will engender a more pronounced flow of eddy currents, consequently yielding a heightened signal response in the detection of cracks and defects [20].

- **The permeability of the material**: Permeability modifications influence the coupling between the coil and the conductive specimen, subsequently impacting the coil's reactance [20].

- **The frequency**: The frequency plays a crucial role in determining the depth to which eddy currents penetrate the material. This penetration is constrained by the skin effect, which signifies that the magnitude of the current diminishes by a factor of 1/e. The skin effect is a phenomenon where alternating currents concentrate near the material's surface due to the counteracting magnetic field generated by the eddy currents, effectively canceling the applied magnetic field. The depth of this surface concentration, referred to as the skin depth, is defined as [20]:

$$\delta = \sqrt{\frac{\rho}{\mu \pi f}} \tag{2.1}$$

In this equation, μ represents the magnetic conductivity of the material, ρ symbolizes the magnetic permeability, and f denotes the frequency. An analysis of this equation leads to the conclusion that lower frequencies are suitable for bulk characterization, while higher frequencies are better suited for surface characterization [21].

2.5.2.2 Application of Eddy Current Sensors in ACSR Cables

ACSR cables are composed of multiple strands, and when exposed to varying magnetic fields, eddy currents are generated around each of these individual strands. These eddy currents encircling each strand confine the flow of magnetic flux into the core of the strand. This characteristic allows for the detection of defects, whether they occur in the outer aluminum strands or the inner steel strands [17].

It's important to note that there are differences in how these two materials, steel and aluminum, respond to eddy currents due to their magnetic properties.

Steel is a ferromagnetic material, which means it exhibits strong magnetic properties when exposed to an external field and retains magnetism even in the absence of an external field. The interaction between the eddy currents and the retained field can result in complex and sometimes unpredictable signal responses. This can potentially mask or distort flaw signals due to magnetic effects. In addition, eddy currents tend to penetrate deeper in ferromagnetic materials due to the material's ability to concentrate magnetic fields [22].

In contrast, aluminum is a non-ferromagnetic material that exhibits weak or negligible responses to magnetic fields and does not become magnetized in the same way as ferromagnetic materials. With fewer magnetic interactions to consider, these materials generally produce simpler and easier to interpret signals. Due to the weaker magnetic effects, eddy currents have shallower penetration depths, limiting their ability to detect defects further below the surface [22].

For the eddy current testing of ACSR cables, coil-based sensors are typically employed. In this context, with "R" representing the coil radius and "r" denoting the strand radius, the induced voltage in the coil is expressed as:

$$V = -\frac{\partial \Phi}{\partial t} \tag{2.2}$$

$$V = -\mu_0 H_0 \omega \cos(\omega t)(\pi R^2 - \pi r^2) \tag{2.3}$$

Where μ_0, H_0, ω, t represent permeability of free space, magnetic field, angular frequency, time.

To achieve the objective, it is possible to eliminate the component of the induced voltage associated with the coil by utilizing an identical but opposing phase compensation voltage (V_C):

$$V_m = V - V_C \tag{2.4}$$

$$V_m = -\mu_0 H_0 \omega \cos(\omega t)(\pi r^2) \tag{2.5}$$

As mentioned earlier, the frequency plays a pivotal role in controlling the skin penetration of magnetic flux, and it's essential to take into account the skin depth denoted as δ. Consequently, the flux that penetrates the strand (Φ_P) is determined by the equation:

$$\Phi_P = \pi r \mu_0 \mu_r \delta H_0 (\sin \omega t + \cos \omega t) \tag{2.6}$$

Where μ_r represents the relative permeability of the strand.

If another coil, referred to as the pick-up coil, is introduced to the sensor, this flux will induce a voltage on the coil, denoted as V_P, which can be expressed:

$$V_P = \pi r \mu_0 \mu_r \delta H_0 (\sin \omega t - \cos \omega t) \tag{2.7}$$

$$V_P = \mu_0 \omega H_0 \pi r^2 [(1 - \frac{\delta}{r}) \sin \omega t + \frac{\delta}{r} \cos \omega t] \tag{2.8}$$

This deduction was based in the bibliography [17, 18].

Since ACSR cables are structured with aluminum on the outside and steel on the inside, it becomes

imperative to choose the optimal inspection technique for this application to maximize the sensor's effectiveness.

2.5.2.3 Inspection techniques

Basic eddy current sensors typically operate at a single frequency, a method widely employed, particularly for detecting surface and near-surface defects. The inducing signal is usually sinusoidal, with frequencies ranging from a few hundred Hertz to several megahertz. The choice of frequency depends on the material and the defect's location. However, this single-frequency technique is limited to inspecting a single layer. To gain deeper insights and reduce irrelevant information, multi-frequency techniques have gained prominence.

Multi-frequency techniques can detect complex-shaped flaws and identify defects even in the presence of variations in conductivity, permeability, geometry, and probe lift-off. These techniques involve the application of excitation frequencies either simultaneously or sequentially. While sequential frequency data processing takes more time, the power available for each frequency is considerably higher than when applied simultaneously. Multi-frequency techniques have also proven effective for testing ferromagnetic materials, outperforming single-frequency methods.

Pulsed Eddy Current (PEC) is an emerging technology in eddy current inspection. PEC-based sensors offer the ability to assess a wide range of parameters, including defect size and location, due to their broad frequency band, particularly rich in low frequencies. This capability allows for subsurface inspection. PEC techniques involve driving a substantial pulsed current into the excitation coil, resulting in transient changes that induce eddy currents in the sample. These eddy currents are then scattered back to the surface by material discontinuities in conductivity and permeability. PEC systems have been developed to perform thickness measurements at significant lift-off distances, making them suitable for corrosion inspection under insulation. As a result, PEC offers greater penetration depth compared to previous techniques. However, PEC systems are not yet widely adopted due to the ongoing development of the analysis of their transient responses.

In addition to choosing the most suitable inspection method for a given application, it is crucial to analyze the resulting inspection data thoroughly and effectively.

2.5.2.4 Data Analysis Techniques for ACSR Cable Inspection

Data obtained from eddy current methods can be analyzed in various domains, including time, frequency, or impedance. Given that eddy current methods primarily rely on changes in coil impedance, impedance plane analyzis is the most common approach for the majority of single-frequency and multi-frequency inspection techniques.

Electrical impedance (Z) represents the total opposition that a circuit presents to an alternating current. Impedance, measured in ohms, encompasses components like resistance (R), inductive reactance (X_L), and capacitive reactance (X_C). Eddy current circuits typically consist of only R and X_L compo-

nents [23]. In the absence of a nearby conductor, the impedance is as follows:

$$Z_0 = R_0 + jX_0 \tag{2.9}$$

In this context, R_0 represents the real part of Z_0, and $jX_0 = j2\pi f_0 L_0$ represents the imaginary part, which is directly proportional to the frequency and the induction coefficient. When a conductor is brought near or passes through the coil, the interaction between the magnetic field of the coil and the eddy currents leads to an impedance denoted as Z_1.

$$Z_1 = R_1 + jX_1 \tag{2.10}$$

Where R_1 and $jX_1 = j2\pi f_1 L_1$ represent the real and imaginary parts of the impedance of the coil near the conductor, denoted as Z_1.

As the coil impedance is a two-dimensional variable, it can be represented in a plane, with the real part (R) along the x-axis and the imaginary part (X) along the y-axis. The impedance Z_1 can be normalized and redefined as [22]:

$$Z_N = R_N + jX_N \tag{2.11}$$

$$Z_N = \frac{R_1 - R_0}{X_0} + j\frac{X_1}{X_0} \tag{2.12}$$

In the impedance plane, R_N is 0 when there's no change in real impedance, and X_N indicates how the impedance with a nearby conductor compares to an "empty" coil. At the "air point" (P_0) with no conductor, $R_N = 0$, and $X_N = 1$.

Material differences play a role: steel being ferromagnetic and aluminum not. When non-ferromagnetic materials approach the coil, they induce eddy currents, creating a liftoff line in the impedance plane. Cracks cause $R_{1+cracks}$ to decrease and $X_{1+crack}$ to increase, but for low-conductive materials, distinguishing lift-off from defects is challenging.

In the presence of ferromagnetic materials, the normalized reactance (X_N) is above 1, akin to non-ferromagnetic materials with cracks.

The zinc layer on steel strands affects impedance due to its negative magnetic permeability. Analyzing the impedance plane helps detect cracks, assess their dimensions, evaluate zinc layer corrosion, and measure thickness. This analysis streamlines maintenance, reducing unnecessary cable replacement and enhancing worker safety.

However, when using PEC systems, it is more appropriate to employ frequency or time domain analysis. In the time domain, the peak amplitude is used to determine the flaw's size, while the time-to-zero crossing is used to assess the flaw's depth (or the thickness of the zinc coating). Deeper flaws result in a longer time to zero crossing. The time to zero crossing and the phase at two different frequencies are also used to determine the depth, length, and height of flaws [20].

Furthermore, research is being conducted on the integration of neural network-based solutions for multi-frequency systems, which offer an alternative to numerical and analytical solutions that require substantial computational power. In testing plates, this method provides good approximations of flaw

size and location, using features such as the maximum amplitude response and the frequency at which the maximum amplitude occurs [20].

2.5.2.5 Sensor Design

Eddy current sensors come in different configurations, such as those with a single coil handling both excitation and detection or designs with multiple coils dividing these functions.

- **Absolute Coils:** These sensors employ a single coil for generating eddy currents and detecting changes in the field. They are widely used due to their versatility. However, absolute probes are sensitive to factors like conductivity, permeability, and liftoff, which need to be minimized for accurate results.
- **Differential Probes:** Differential probes consist of two coils, often wound in opposition. When both coils are over either a defect or an intact area, they produce no differential signal. However, if one coil is over a defect while the other is not, a differential signal is generated. These probes excel in sensitivity to defects but may not be as responsive to slowly changing features. They also tend to reduce wobble signals. However, they can pose challenges when defects are wider than the space between coils.
- **Reflection Probes:** These probes also feature two coils, similar to differential probes, but they are not wound together. One coil is dedicated to excitation, and the other is used for detection. The advantage of this design is the separate optimization of both coils. For example, the excitation coil can be dimensioned to produce a strong, uniform flux field, while the pickup coil can be tailored to be sensitive to very small defects.

These probe designs offer various advantages and considerations, depending on the specific requirements of the inspection task.

Chapter 3

Implementation

3.1 Robot prototype

In line with the motion objectives outlined in Section 1.3, we employed the robot illustrated in figure 3.1 as an initial model for subsequent robot motion analysis.

Figure 3.1: Robot Prototype

This prototype comprises a chassis equipped with controllers connected to the motors at the rear of the robot, directly linked to the front traction wheels. These traction wheels are 3D-printed U-groove wheels with gear-like features. Positioned beneath the front section of the robot are four support wheels that can be adjusted to compress the line between the traction and support wheels. Additionally, a counterweight was incorporated to enhance the robot's stability.

As the trials were exclusively conducted on the test line, this prototype features wired communication, with the battery positioned on the ground. For actual inspection operations, the prototype would necessitate the addition of a battery box, two PCs (one mounted on top of the battery box and the other on the ground, communicating via Wi-Fi), a sensor, which will be discussed later in this chapter, and an encoder for precise robot control. Figure 3.2 offers a comprehensive hardware diagram of the robot.

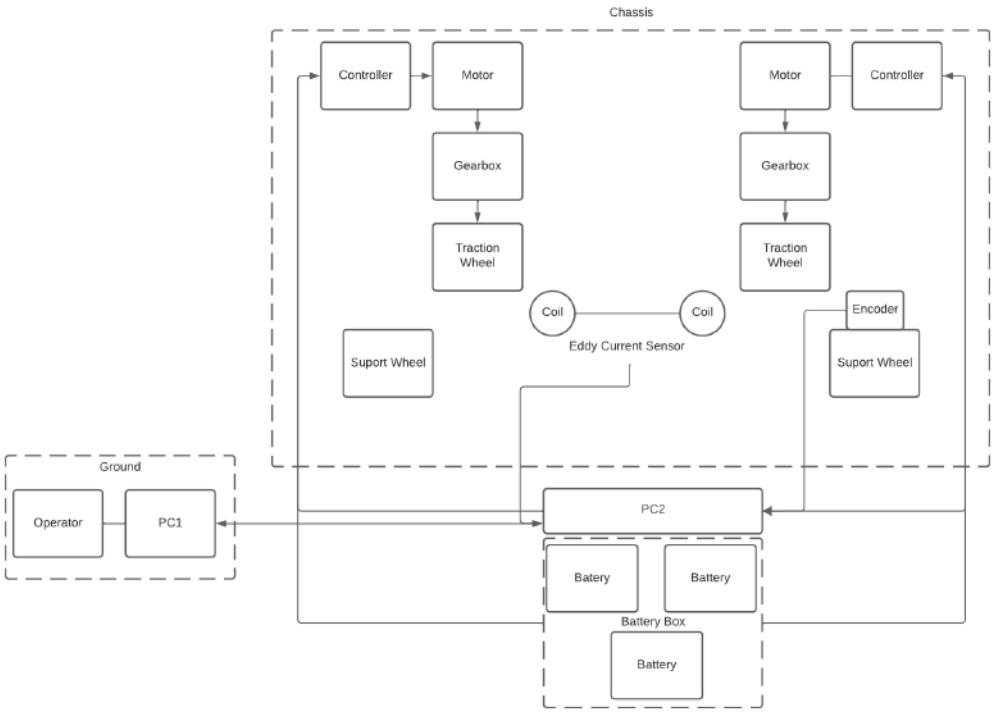

Figure 3.2: Hardware diagram

3.1.1 U-groove Wheels

Traction is the term used to describe how effectively a wheel or tire grips a surface. It depends on the number of contact points between the wheel and the conductor, meaning that the more contact points, the better the wheel's traction.

Since U-grooved wheels are not readily available in small quantities, 3D printing was used to create the traction wheels for the prototype. Careful consideration was given to the dimensions of these custom wheels. The wheel diameter was determined by considering the dimensions of the space damper. As the robot moves, its wheels come into contact with the space damper at point P. The torque of the motor (T), which is directly connected to the wheel shaft, exerts a traction force (R) and a normal force (N) at point P. The following deduction was adapted from reference [24].

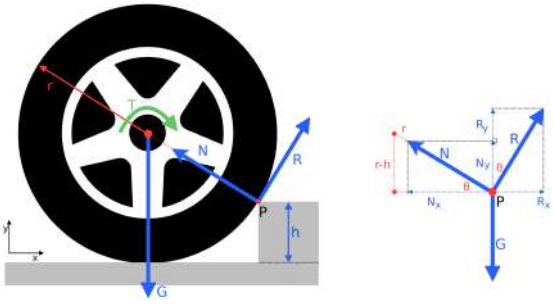

Figure 3.3: Forces applied on point P

Analyzing figure 3.3, the equilibrium equation at point P on the x-axis can be represented as shown in equation 3.1:

$$\sum Fx = 0$$

$$R_x - N_x = 0$$

$$R \cdot \cos(\frac{\pi}{2} - \theta) = N \cdot \cos(\theta)$$

$$R \cdot \sin(\theta) = N \cdot cos(\theta) \tag{3.1}$$

Solving Equation 3.1 for the normal force (N) yields:

$$N = R \cdot \frac{\sin(\theta)}{\cos(\theta)} \tag{3.2}$$

Now, considering the equilibrium equation at point P on the y-axis 3.3:

$$\sum F_y = 0$$

$$R_y + N_y - G = 0$$

$$R_y + N_y = G$$

$$R \cdot \cos(\theta) + N \cdot \sin(\theta) = G \tag{3.3}$$

Where G represents the gravitational force.

Solving for the traction force (R) results in:

$$R = G \cdot \cos(\theta) \tag{3.4}$$

Observing figure 3.3 , it is possible to calculate the angle theta (θ) using the equation:

$$\sin(\theta) = \frac{(r - h)}{r} \tag{3.5}$$

Finally, after calculating the value of R, it is possible to determine the necessary diameter of the wheel to overcome the obstacle using the equation:

$$r \geq \frac{T}{R} \tag{3.6}$$

Considering the torque characteristics of the motors in use, it was determined that two different wheel sizes, 160mm and 200mm, would be produced. In addition to varying the diameter, it was imperative to define the groove's depth, width, as well as the dimensions of the STD keyway and the shaft diameter to ensure compatibility with both the motor and conductor. The specified dimensions can be found in table 3.1.

Table 3.1: Trial wheels dimensions (mm)

(a)	160	200
(b)	3x4	3x4
(c)	80	120
(d)	12	12
(e)	50	50
(f)	40	40

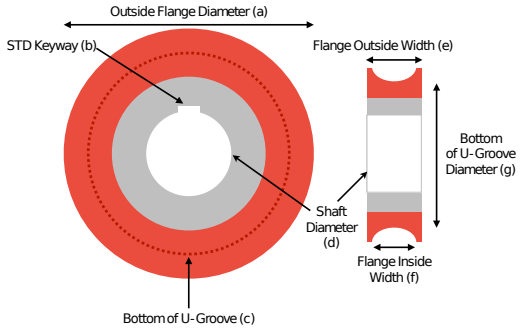

Figure 3.4: U-groove wheels measurements

The choice of material for 3D printing also significantly impacts traction. In table 3.2, you can find a qualitative assessment of rolling resistance, floor surface preservation, and wear resistance for various levels of hardness. This evaluation is adapted from sources cited in [25, 26].

Table 3.2: Material hardness characteristics

Hardness [shore A]	Rolling resistance	Surface preservation	Wear resistance
60	Good	Excellent	Satisfactory
65	Very Good	Very Good	Satisfactory
70	Good	Good	Very Good
75	Very Good	Good	Very Good
82	Very Good	Very Good	Very Good
92	Excellent	Good	Excellent

The Shore A scale is commonly used to categorize soft to medium-soft materials based on their hardness. Examples of such materials include rubber, which is commonly used to increase traction in similar applications [27].

Based on the study, it was decided to 3D print two tires for the wheels, one with 82 Shore A TPE filament (orange) and the other with 92 Shore A TPU filament (white). These specific hardness values were chosen because low rolling resistance was a priority. While surface preservation is important, superior rolling resistance outweighs any compromise in surface preservation, especially with the TPU filament. The 3D-printed wheels are illustrated in Figure 3.5.

(a) (b)

Figure 3.5: Printed 3D wheels: (a) 160mm wheel; (b) 200mm wheel.

Testing was carried out with the 160mm wheels.

These covers were intended to replicate the function of gear teeth when they come into contact with

the space damper. To achieve this, it was necessary for the distance between the teeth to be equal to the height of the space damper section that makes contact with the wheels, which was measured to be 2 cm. To calculate the required angle to create an arc length of 2 cm, the equation in 3.7 was applied.

$$\text{Arc length} = 2\pi r \frac{\theta}{360} \tag{3.7}$$

The model of the cover, is depicted in figure 3.6.

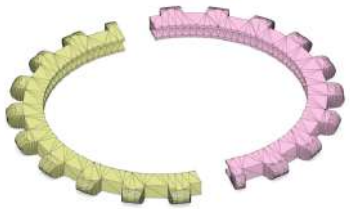

Figure 3.6: Gear wheel cover

3.2 Robot motion and obstacle surpassing trials

This trial consists of attaching the robot to the line, making it run the line, and observing if it is able to overcome the space dampers, go up the slope without slipping, and come down the slope without gaining too much speed while evaluating stability throughout the course.

3.2.1 Test line

High-voltage overhead power lines typically consist of a multi-phase alternating current circuit and rely on support from numerous metal poles positioned along their route. The conductors responsible for transmitting electricity are typically constructed from aluminum or steel-reinforced aluminum. These conductors can be organized into single, double, triple, or quadruple bundles.

The line segments between the various poles incorporate various elements, including vibration dampers and space dampers, which are used in bundles containing more than two conductors. These space dampers are positioned approximately 50 meters apart, serving a dual purpose of cooling and preventing detrimental oscillations or contact between cables within the same bundle. Managing this interaction poses a significant challenge for the robot.

To facilitate testing and experimentation with the robot, REN has provided a dedicated test line located in Palmela, as illustrated in Figure 3.7.

In Palmela, the conductor, as depicted in Figure 3.7(a), is constructed from an ACSR (Aluminum Conductor Steel Reinforced) cable. It comprises seven steel wires with a diameter of 2.32mm, arranged in two concentric layers. These steel wires are surrounded by 42 hard aluminum wires with a diameter of 4.14 mm, distributed across three concentric layers. The robot will traverse on the outermost layer of these aluminum wires [28]. In the middle of this test line is a space damper, shown in figure 3.7(b).

(a)

(b)

Figure 3.7: Test line, Palmela: (a) Span for trials; (b) Space damper.

3.3 Speed and traction control simulation

To gain a better understanding of the ”robot-motor” system and to test the speed and traction control algorithms, a Simulink model was created using the motor motion equations and the mechanical characteristics of the robot. The equations of motion for the motor are presented in equations 3.8 and 3.9.

$$\frac{\partial i}{\partial t} = \frac{-R}{L}(i) - \frac{K_b}{L}(\omega_m) + \frac{1}{L}V \tag{3.8}$$

$$\frac{\partial \omega_m}{\partial t} = \frac{k_m}{J}(i) - \frac{b}{J}(\omega_m) - \frac{f_c}{J}(\omega_m) - \frac{T_d}{J} \tag{3.9}$$

Where:

i = Current	V = Input voltage
t = Time	k_m = Size constant
R = Rotor resistance	J = Moment of inertia
L = Rotor inductance	f_c = Friction factor
k_b = Back emf constant	b = Viscous friction coefficient
ω_m = Angular velocity	T_d = Disturbance torque

The size constant and back emf constant can be calculated by the equations 3.10 e 3.11

$$k_m = \frac{k_T}{\sqrt{R}}; \tag{3.10}$$

$$k_b = \frac{1}{k_v} \tag{3.11}$$

Where:

k_T = Torque constant	k_v = Speed constant

The values utilized are depicted in Table 3.3, sourced from the datasheet of the Maxon motors' brushless motor model EC90 represented in figure A.1 in appendix A. All the values were obtained from the datasheet, except for the friction factor. Given that brushless motors generally exhibit minimal friction, attributed to the presence of bearings, we considered a friction factor of $f_c = 0$ for this simulation, as detailed in the source [29].

Table 3.3: Values used in simulation

Parameters	Value	Units
R	0.0577	Ω
L	0.058	mH
k_b	0.004	Vs/rad
k_m	0.148	Nm/A
b	1e-3	(-)
J	0.00317	kgm
f_c	0	(-)

Incorporating the motor parameters is essential, but it's equally important to account for the robot's specific characteristics. Here are the parameters that are factored into the simulation:

$\mu =$ Friction coefficient
$GR =$ Gear ratio
$s =$ Slip ratio
$m =$ Total robot mass
$R_w =$ wheel radius
$F_N =$ Normal force
$Q =$ weight balance factor
$F_T =$ Tire force

In the context of the robot, some parameters had to be approximated during the simulation, as it coincided with the physical testing of the robot. One of these approximations was the weight balance factor (Q), which signifies the weight distribution on the motors. In this case, a value of $Q = 0.5$ was chosen, as the robot employs two motors, and most of its weight is supported by the wheels and, by extension, the motors. Furthermore, the total mass of the robot had to be approximated. The values used are outlined in table 3.4 where the GR value was taken from the datasheet in figure A.2 in appendix A.

Table 3.4: Values used in simulation

Parameters	Value	Units
GR	3.5	(-)
Q	0.5	(-)
R_{wt}	80	mm
R_{ws}	30	mm
m	7	kg

The Simulink implementation of the combined motor and robot parameters, which describes the

system based on equations 3.12 to 3.19, is depicted in figures 3.8 to 3.11.

During the simulation, the motor equations were directly applied by connecting the outputs, which were the current and angular speed, to the input of the gain blocks representing their respective multipliers. This is illustrated in figure 3.8.

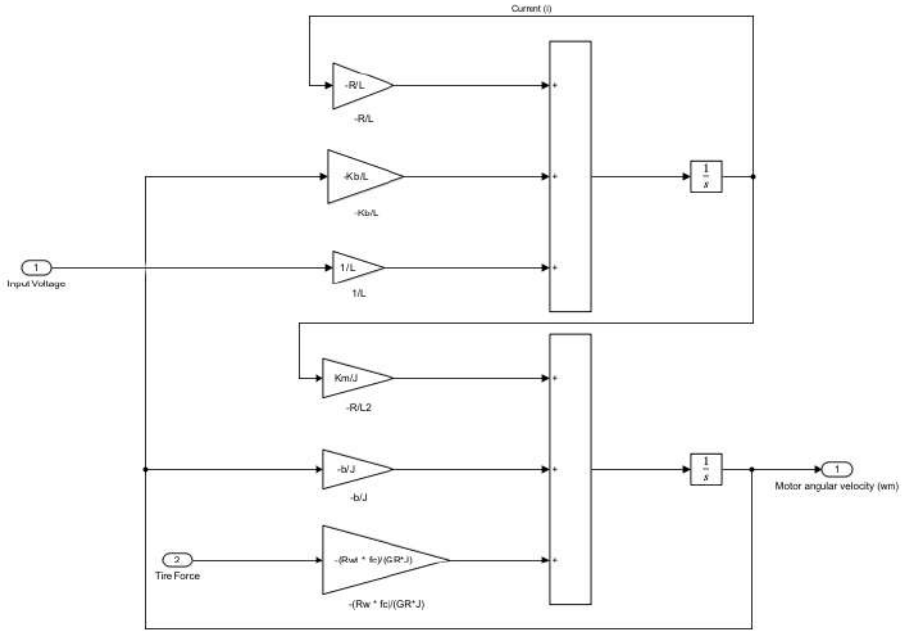

Figure 3.8: Motor model

$$\frac{\partial i}{\partial t} = \frac{-R}{L}(i) - \frac{K_b}{L}(w_m) + \frac{1}{L}V \tag{3.12}$$

$$\frac{\partial w_m}{\partial t} = \frac{k_m}{J}(i) - \frac{b}{J}(w_m) - \frac{R_w \cdot F_T}{GR \cdot J} \tag{3.13}$$

After simulating the motors and obtaining their angular velocities, it was necessary to calculate the speed of the traction wheels. This was done by dividing the angular velocity of the motors by the gear ratio and then multiplying this speed by the diameter of the wheel. Additionally, the speed of the support wheels had to be calculated using equation 3.15.

For this robot, which employs two motors, the traction force (FT) used was the mean of both traction wheels. An integrator block was subsequently employed to derive the velocity value. The simulation method utilized is depicted in figure 3.9.

$$\frac{\partial \theta}{\partial t} = w_m \tag{3.14}$$

$$\frac{\partial v}{\partial t} = \frac{F_T}{m} \tag{3.15}$$

$$\frac{\partial x_p}{\partial t} = v \tag{3.16}$$

Where:

$\theta =$ Angle of the motor $\quad v =$ Robot's speed $\quad x_p =$ Robot's position

Finally, utilizing the previously calculated speeds and referencing equations 3.17-3.19, it is possible to calculate the slip, friction coefficient, and tire force. For the computation of the friction coefficient, a Matlab function block was employed. The implementation in the simulation is illustrated in figure 3.10.

$$\mu = 1.63 \cdot (1 - e^{-27 \cdot s}) - 0.9 \cdot (1 - e^{-15 \cdot s}) - 0.1 \cdot s \tag{3.17}$$

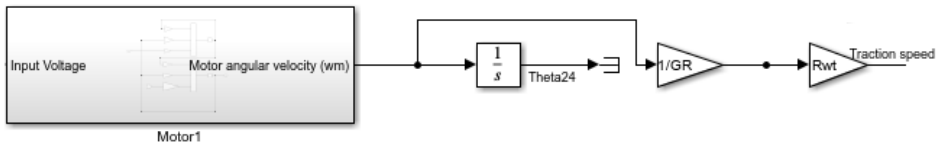

(a)

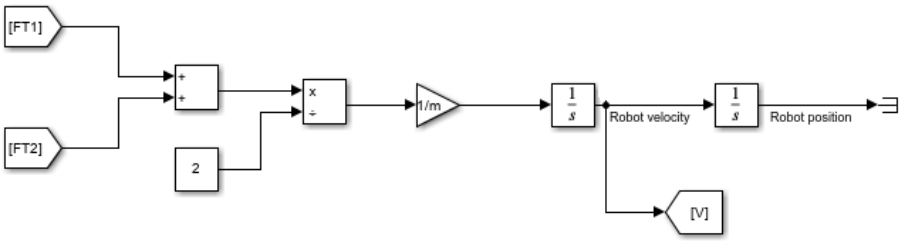

(b)

Figure 3.9: Speed of the wheels: (a) Traction wheel; (b) Support wheel.

$$s = \frac{w_t - w_s}{|w_s| + tol} \tag{3.18}$$

$$F_T = \mu(mgQ) \tag{3.19}$$

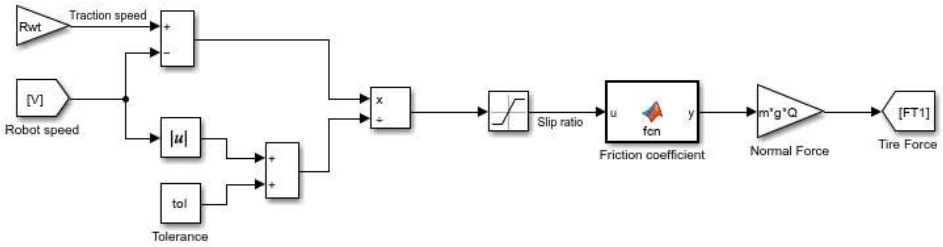

Figure 3.10: Slip, friction coefficient and tire force calculation

With the modeled robot-motor system, it's possible to implement traction and speed control. The speed control is a simple loop control where the speed of the traction wheel is compared to the speed target and then passed through a PID controller. Both wheel speeds must match, so before the final PID, it's necessary to compare both wheel speeds to synchronize them.

The traction control is a switch control loop where the support wheel speed is compared with the speed of the traction wheels. If they match, the control turns off, and a constant block with a zero value is used to simulate the control when shut down. When they don't match, the slip control activates and tries to approximate the slip to 0.01. The speed and traction control loop is shown in figures 3.11.

3.4 Eddy current sensor

As mentioned in section 1.3, the objective of the robot is to detect broken wires inside the cables, internal corrosion, loss of cross-section in the internal wires, and loss of zinc thickness in the internal

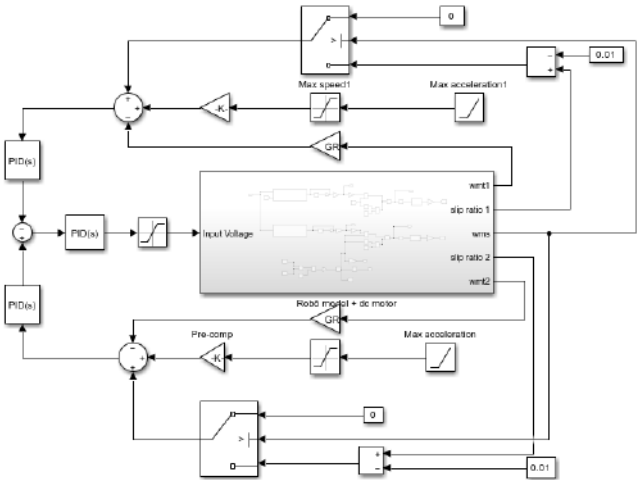

Figure 3.11: Control loop

steel wires. To achieve these objectives, it is necessary to better understand the reactions caused by this type of defect. Since there was no way of creating defects only in inside layers, these tests were focused on laying a baseline for future development of this sensor to implement in inspection work.

3.4.1 Flaw detection: Longitudinal and transversal cuts

The purpose of this first trial is to determine if it is possible to detect cuts in a conductor material using the sensor and circuitry that will be presented later. This trial also aims to gain a better understanding of the perturbations in the coil's voltage and current when it encounters cuts in the conducting material.

The system and circuit used for this test are shown in figure 3.12. It includes a signal generator, an encircling coil, three resistors (two with a value of 100Ω and the other with a value of 1.2Ω), an oscilloscope, and an aluminum tube with an internal diameter of $8mm$ and an external diameter of $30mm$.

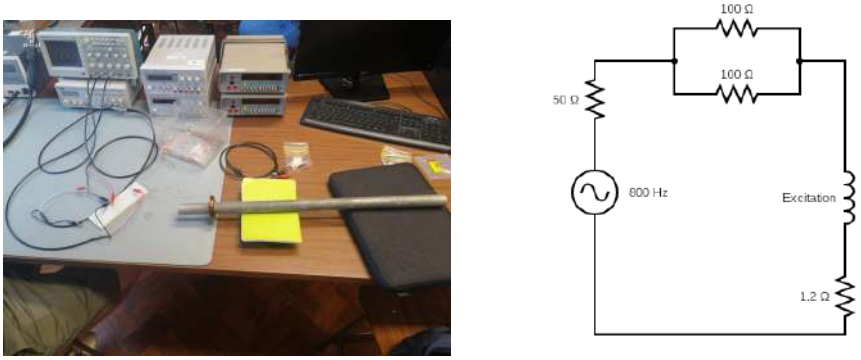

(a) (b)

Figure 3.12: Eddy current test 1: (a) Test bench; (b) Circuit used in the test.

Two parallel resistors were connected in series with the generator to stabilize the current detection. To measure the coil current, the resistor in series with the coil was used, which has a value close to

1Ω. This configuration provided more stable current readings compared to measuring without resistors, which would cause the current to fluctuate significantly.

Three cuts were made in the tube for the experiment. One of them was transverse, with dimensions of $25mm$ in horizontal length and $5mm$ in vertical length, while the other two were longitudinal cuts, each with dimensions of $50mm$ in horizontal length and $5mm$ in vertical length. These cuts are shown in figure 3.13.

(a) Longitudinal cut (b) Transversal cut

Figure 3.13: Test sample

The signal generator was utilized to produce a sinusoidal excitation signal with an amplitude of $8V$. The frequency of the signal was varied from decade to decade. The choice of frequencies was based on the skin depth, as explained in section 2.5.2.1. Ideally, the distance between the defect and the surface should be within one to two skin depths for optimal performance. The selected frequencies and their corresponding skin depths are provided in table 3.5.

Table 3.5: Values of skin depth for each frequency

Frequency	δ [mm]	2δ [mm]
8 Hz	29	58
80 Hz	9	18
800 Hz	3	6
8 kHz	0.9	1.8
80 kHz	0.3	0.6
800 kHz	0.1	0.2
8 MHz	0.06	0.12

The selected test frequencies were $800Hz$, $8kHz$, and $80kHz$. These frequencies were chosen because the cuts were located on the surface and had a depth of 5mm. Frequencies above $80kHz$ were deemed too close to the surface and were considered irrelevant for this test.

The probe used in the test is a circular coil consisting of 426 turns. It has an outer diameter of $37mm$, an inner diameter of $34mm$m resulting on a distance to the conductor of $2.2mm$, and a length of $7mm$. To create the coil, a 3D-printed support was used to wind the copper wire. The coil is depicted in figure 3.14.

To prevent the copper wire from unwinding, the height of the support walls must be greater than the height of the coil. This height was determined using equation 3.20.

$$h = \frac{N}{\frac{L_c}{D_w}} D_w \tag{3.20}$$

Figure 3.14: Coil

The experiment was repeated ten times for each defect and none defect area and frequency. Then, the average of each signal (v, v_1) was used to calculate the difference in amplitude (Δv) for each frequency using Matlab, as shown in equation 3.21.

$$\Delta v = v - v_1 \tag{3.21}$$

The procedure for the current is the same.

3.4.2 Flaw detection: Corrosion

For this trial, the main objective is to determine if it is possible to detect corrosion and to understand if there is a difference in the sensor's response.

The material used in this experiment is the same as in the first one, except for the test sample. Instead of a tube with cuts, the sample has surface corrosion, as shown in Figure 3.15. The measurement of

Figure 3.15: Test sample

the values of voltage and current followed the same method as well as the data analysis.

3.4.3 Flaw detection: Cuts in only one layer of aluminum

This test is aimed at detecting broken strands in the first layer of aluminum. Since defects in the strands within the lines can have various orientations, not limited to just longitudinal or transverse, the sensor's capability to detect broken strands with different cutting directions was tested. Four cuts were made in the sample, each at an angle of $-45°$, $0°$, $45°$, and $90°$, as illustrated in figure 3.16.

The experimental setup and methodology were consistent with the previous experiments, with the exception of the coil's diameter. As the ACSR cable comprises concentric layers of twisted strands, when the cable cuts were made, the cable started to unravel, and the previous inner diameter of the coil became smaller than the diameter of the cable. Consequently, a coil with an inner diameter of $38mm$,

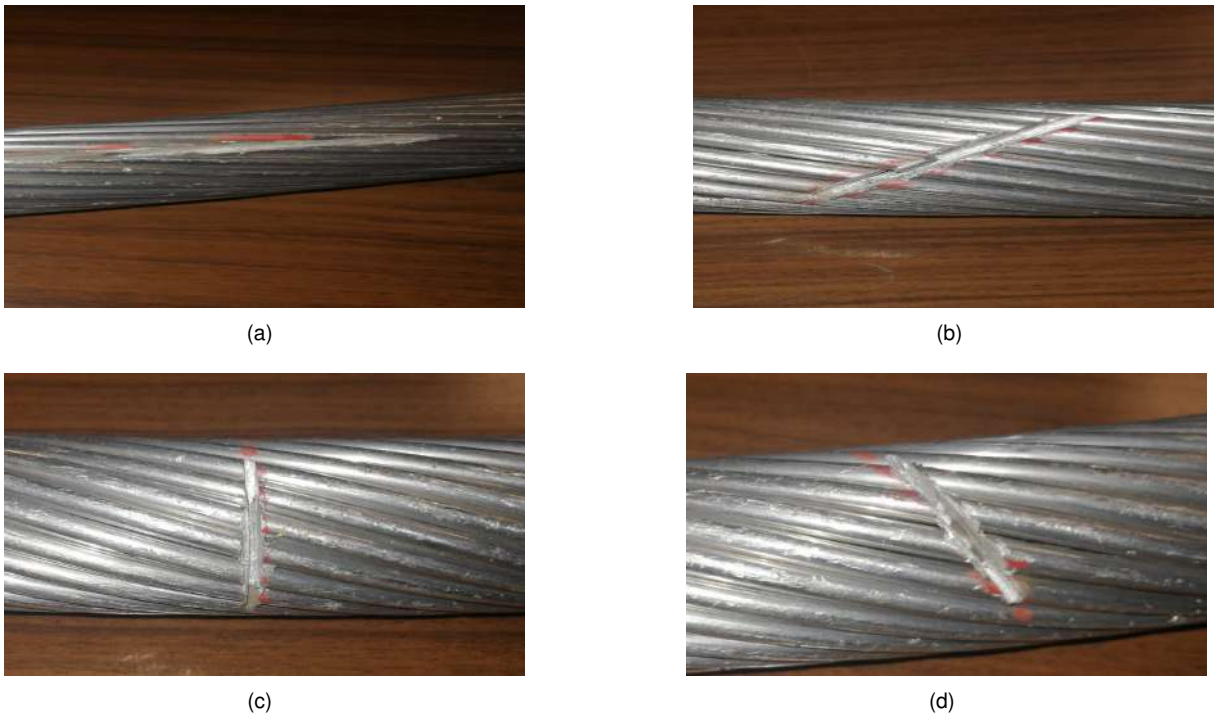

(a) (b)

(c) (d)

Figure 3.16: First layer cuts: (a) $0°$; (b) $45°$; (c) $90°$; (d) $-45°$.

resulting on a distance between the coil and the cable of around 4mm due to the unravel of the cable, and an outer diameter of $41mm$ was used.

Given the change in coil diameters, a new support was required. Using equation 3.20 to calculate the support height, a modification was needed. Due to calculation errors, it was necessary to cut the wire to ensure it would fit within the support, resulting in a coil with fewer turns.

3.4.4 Flaw detection: Cuts in more than one layer of aluminum

The objective of this trial was to study the differences in the detection of more than one layer of broken aluminum. This was done to understand which frequencies detect each layer of the ACSR cable, as the cable's structure makes it impossible to predict using the skin depth. Cuts were made, adding one extra broken layer until they reached the steel layer. It was uncertain if the cable would stay together if the steel wires had been cut. The cable used is shown in figure 3.17.

Figure 3.17: Cable with cuts two layers (right), and three layers (left) deep.

The bench setup and methodology were the same as in the experiment in section 3.4.3.

Chapter 4

Results

In this chapter, it will be presented the discussion of the results that were obtained during the trials.

4.1 Robot motion and obstacle surpassing trials

4.1.1 Hand trial

A manual test was conducted to evaluate the actual interaction between the wheels and the space damper before integrating them into the robot. In this trial, a rigid rod was inserted into the central axis of the wheel, and various forces were applied to assess traction and estimate the torque required to overcome the space damper. This test served a dual purpose: understanding the force needed from the wheels and determining the optimal size to avoid unnecessary filament waste.

During the manual trial, both the 160mm and 200mm wheels demonstrated relatively low force requirements for ascending the obstacle. The 200mm wheel required slightly less force, although the difference was not considered significant. However, it was observed that the 200mm wheel exhibited reduced stability when positioned on top of the space damper compared to the 160mm wheel. Regarding the tire material, both demonstrated a satisfactory level of traction along the test line, with no noticeable difference in the force requirements for climbing. As a result, the decision was made to utilize the 160mm wheel with TPE 82 Shore A material. This choice was motivated by faster printing times and reduced filament consumption.

4.1.2 Robot Movement trial

Following the integration of the new wheels into the prototype, a trial was conducted, demonstrating the effectiveness of the counterweight support in maintaining the robot's stability, even when encountering significant disturbances on the line.

In terms of stability, the wheels displayed some instability due to factors such as the relatively wide groove width, and the wheel's low weight.

The prototype's impressive traction was attributed to the tire material and the number of contact points, resulting in an improved coefficient of friction and enhanced traction capacity. The robot effectively ascended slopes, only experiencing pauses when facing the space damper. During traction evaluation, the prototype was programmed to move in both directions, and the displacement between the starting and ending points was measured. It was observed that as the robot ascended higher, the displacement increased, although it never exceeded 16 centimeters.

The section of the space damper utilized for wheel propulsion has a 20mm height, leading to the decision to space the teeth 20mm apart. The wheel exhibited sufficient traction and force to overcome the obstacle. However, an issue arose when the wheel's teeth became entangled in the space damper, causing the wheel to become stuck. During such incidents, the second wheel lacked the necessary traction to move it forward.

As a solution, a rubber-based paint was applied to the robot's tires to enhance their grip when encountering this specific obstacle. This modification aimed to enable the robot to navigate the obstacle successfully but required the robot to remain in a straight orientation. Any deviation in the robot's alignment, especially when its wheels passed over the obstacle, caused the wheels to lose contact with the conductor, making it challenging for the robot to continue. This situation underscores the importance of maintaining the robot's orientation when dealing with the obstacle and considering factors like environmental conditions and the robot's inclination when implementing modifications to improve its performance. Additional adjustments and strategies may be necessary to ensure reliable traversal under various circumstances.

This trial indicates that while this prototype closely emulates a real-line suspended robot, practical implementation may require adjustments such as increasing the wheel weight and reducing the groove width to bring it closer to the line. The main concern revolves around obstacle navigation. To consistently overcome the obstacle, implementing an active balance mechanism may be necessary. While the rubber paint improved traction and allowed the robot to navigate the obstacle successfully, it was observed that the paint could transfer onto the conductor, potentially interfering with the robot's motion. Therefore, an alternative method should be considered to enhance the tires without causing this transfer of paint.

4.2 Speed and traction control simulation

The analysis of both plots, presented in Figure 4.1, reveals several noteworthy observations. Prior to the implementation of traction control, there was a minor degree of wheel slip, which is expected given the robot's relatively modest speed. However, minimizing slip is crucial, and the introduction of this control method effectively addressed the issue.

Furthermore, the plots illustrate that before the control's implementation, the robot underwent rapid acceleration, achieving its maximum speed in less than one second. Following the implementation of the control, a noticeable shift toward smoother acceleration occurred, with the robot reaching its full speed in two seconds. This improved acceleration profile offers several advantages, especially in the context of the sensor's inspection capabilities. Abrupt accelerations can introduce instability, increasing the risk

of the robot losing balance and potentially falling.

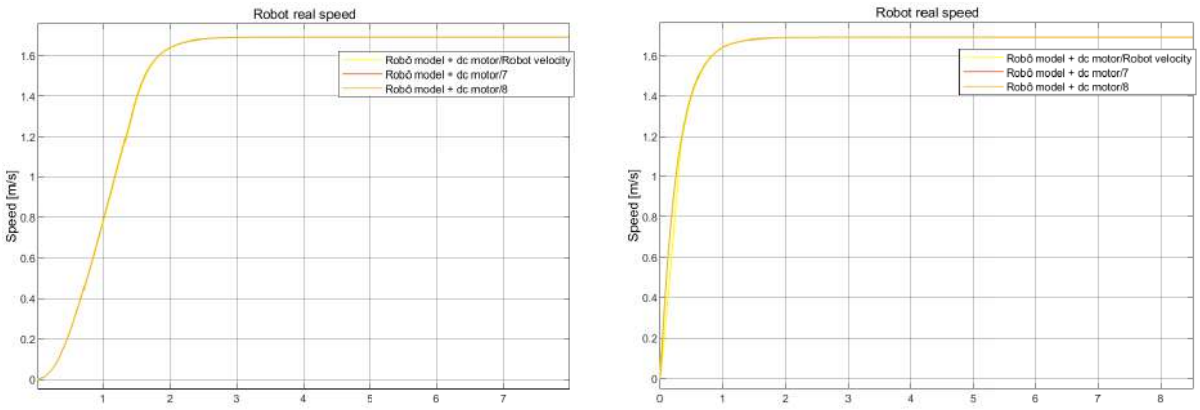

(a) (b)

Figure 4.1: Real speed of the wheels: (a) With traction control; (b) Without traction control.

4.3 Eddy current sensor

This section will feature the presentation and interpretation of graphs depicting the current characteristics of the coil utilized in the sensor trials.

4.3.1 Flaw detection: Longitudinal and transversal cuts

The method employed involved a direct analysis of the current, as it is understood that defects lead to impedance perturbations in the coil, resulting in a reduction in coil current. Figure 4.2 presents the plots of the coil current as it traverses the defect-free sections of the test.

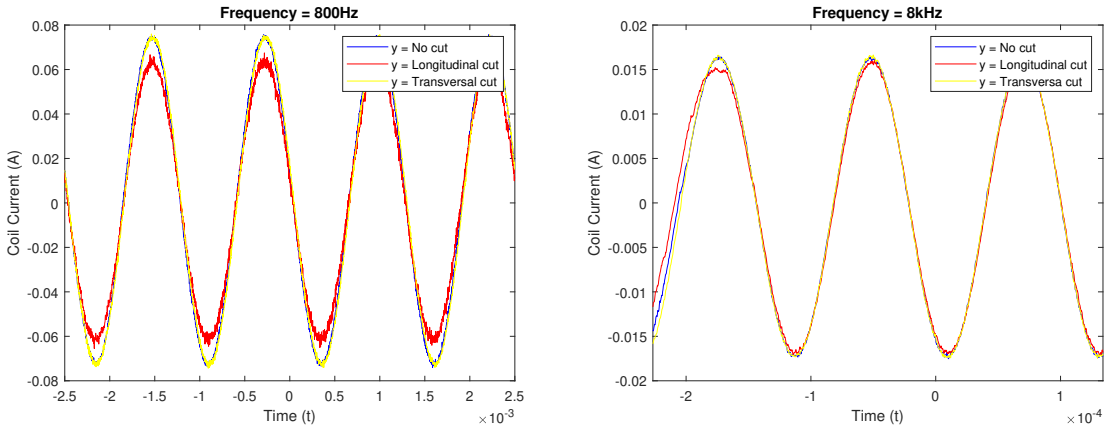

(a) (b)

Figure 4.2: Coil current: (a) 800Hz; 8kHz.

Variations can be observed in both the 800Hz and 8kHz plots. Upon a preliminary examination, it becomes apparent that at 800Hz, the longitudinal cut is detected, while the transversal one is not.

This result aligns with expectations based on information from the literature, indicating that the coil's orientation renders it unable to detect the transversal cut.

However, to perform a more comprehensive assessment of the 8kHz data, it is necessary to scrutinize the values presented in table 4.1.

For the 80kHz frequency, obtaining precise values from the oscilloscope was challenging due to the extremely low currents.

Table 4.1: Coil current variations

Frequency	Current variation [mA]			Current variation [%]		
	Longitudinal cut	Transversal cut	Reference	Longitudinal cut	Transversal cut	Reference
800Hz	7.5	0.13	2	9.64	0.17	2.17
8kHz	0.61	-0.31	0.4	3.81	1.94	1.97

To establish a reference value, the mean of the voltage variation readings when the coil was free of defects was calculated for all frequencies in every trial. This allowed for differentiation between actual flaw detection and noise in the data.

The values in the table corroborate the earlier conclusion for the 800Hz frequency, as the observed variation corresponds to approximately a 10% change, whereas the noise level was around 2%. This suggests that the longitudinal cut is indeed detected at 800Hz, consistent with our initial assessment.

However, at 8kHz, the variation is almost twice the level of noise, which, in a real-world scenario, might warrant further inspection of that particular frequency range. Nevertheless, the results are not conclusive enough to definitively assert the presence of a defect.

This test has provided valuable insights into the behavior of eddy currents, with particularly promising results at the 800Hz frequency.

4.3.2 Flaw detection: Corrosion

The current signals for the same frequencies as in the prior trial are presented in Figure 4.3.

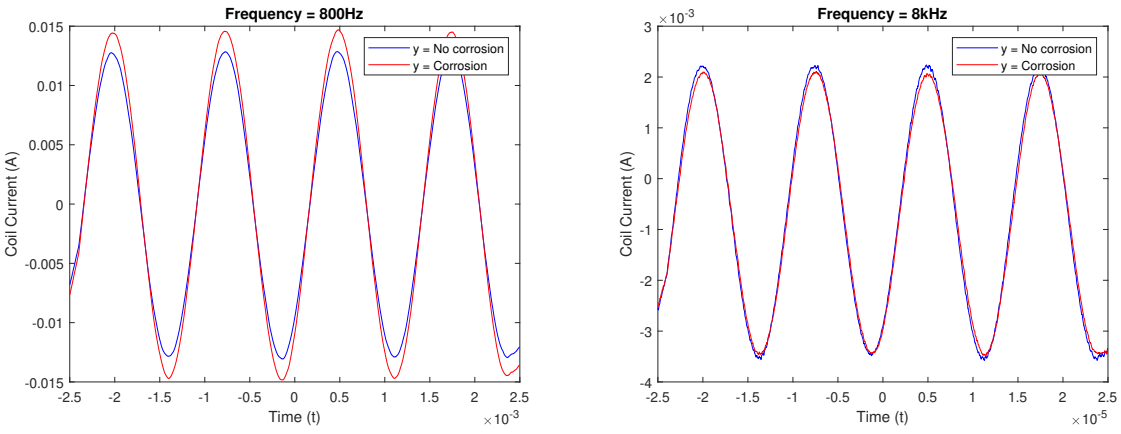

(a) (b)

Figure 4.3: Coil current: (a) 800Hz; (b) 8kHz.

It's evident that the maximum current varies because the test sample materials differ. Unfortunately, the specific material of the tube remains uncertain, as it was obtained from a school and lacked proper labeling. As a result, an accurate calculation of the skin depth was not feasible, and the same frequencies were retained for consistency.

Visual examination suggests that corrosion may have been detected at 800Hz.

At 8kHz, there is a more noticeable variation, but to draw a definitive conclusion, it's imperative to analyze the results presented in table 4.2.

Table 4.2: Coil Current variation

Frequency	Current variation [mA]		Current variation [%]	
	Corrosion	Reference value	Corrosion	Reference value
800Hz	1.73	0.29	11.8	2.33
8kHz	0.13	0.03	6.17	1.9

In this trial, the maximum current is noticeably lower, and the absolute variation in terms of mA is considerably reduced. However, when compared to the reference value in terms of a percentage, it is possible to conclude that there is a detection for the 800Hz trials, as a roughly 10% variation in voltage seems to be a sufficient indicator of a defect.

For the 8kHz trials, the observed variation when passing over corrosion is approximately 3.2 times higher in percentage terms. This significant percentage difference strongly supports the assumption that there is a defect in that particular section of the tube

4.3.3 Flaw detection: Cuts in only one layer of aluminum

Due to the complexities arising from inter-strand spaces and the complex geometry of ACSR cables, accurately calculating skin depth became challenging. As a result, we retained the same frequencies for consistency. The current values are presented in figures 4.4, 4.5, and 4.6.

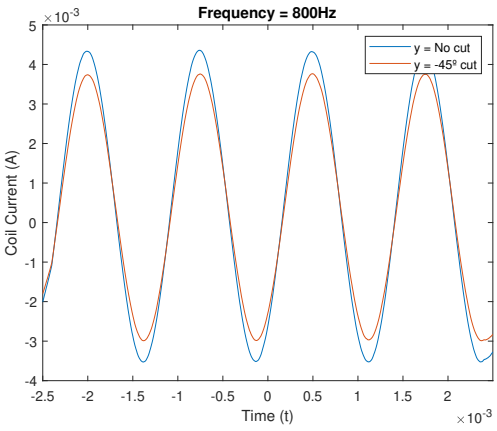

(a)

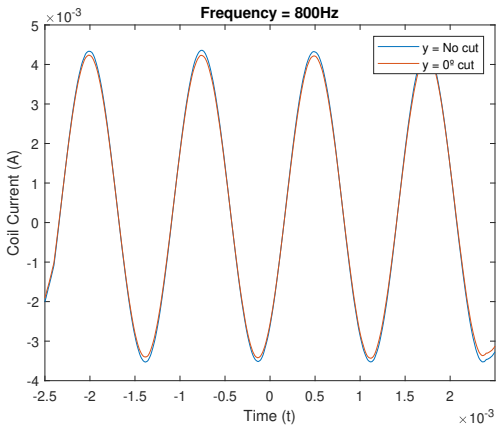

(b)

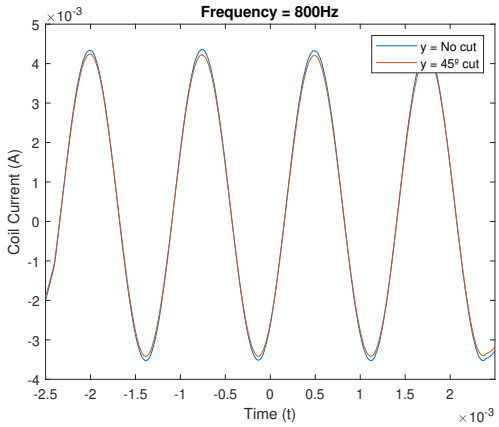

(c)

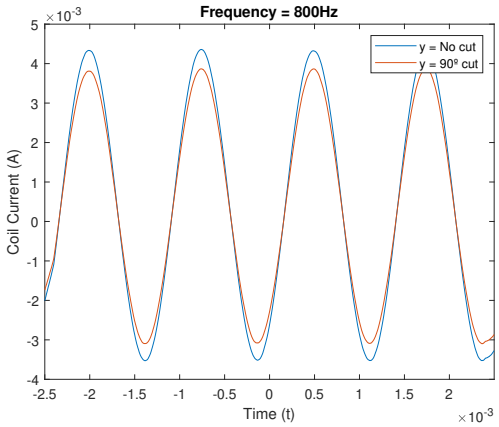

(d)

Figure 4.4: Coil current 800Hz with cuts of: (a) $-45°$;(b) $0°$;(c) $45°$; (d)$90°$.

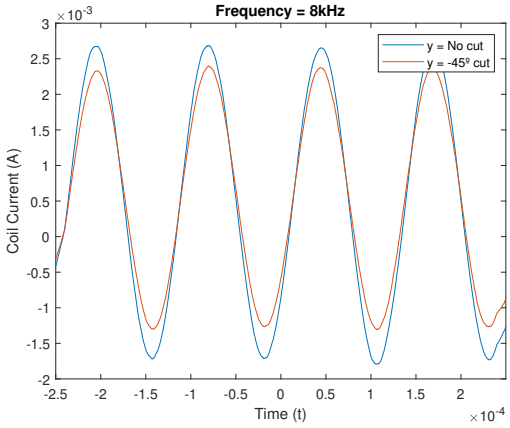

(a)

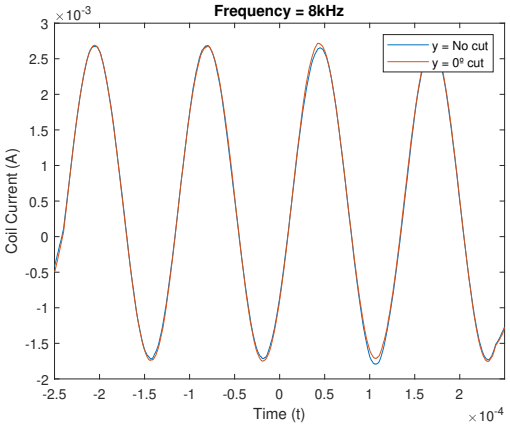

(b)

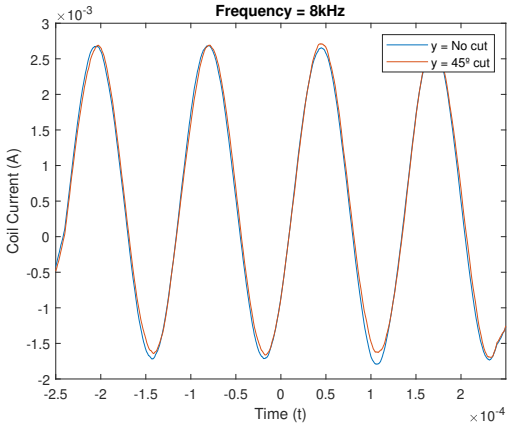

(c)

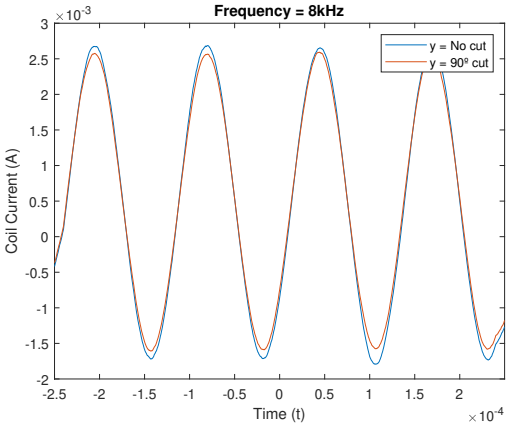

(d)

Figure 4.5: Coil current 8kHz with cuts of: (a) $-45°$; (b) $0°$; (c) $45°$; (d) $90°$.

In this scenario, analyzing figure 4.4, it is evident that the type and orientation of the cut significantly influence the current variation. Notably, the $-45°$ cut induces the most pronounced variations, while the

$90°$ cut exhibits a more shallow effect. Conversely, the $0°$ and $45°$ cuts do not appear to be detected.

At 8kHz, the results mirror those at 800Hz, with the $-45°$ cut exhibiting the highest variation. The $90°$ cut still shows a relatively shallow variation, while the $0°$ and $45°$ cuts do not display significant changes.

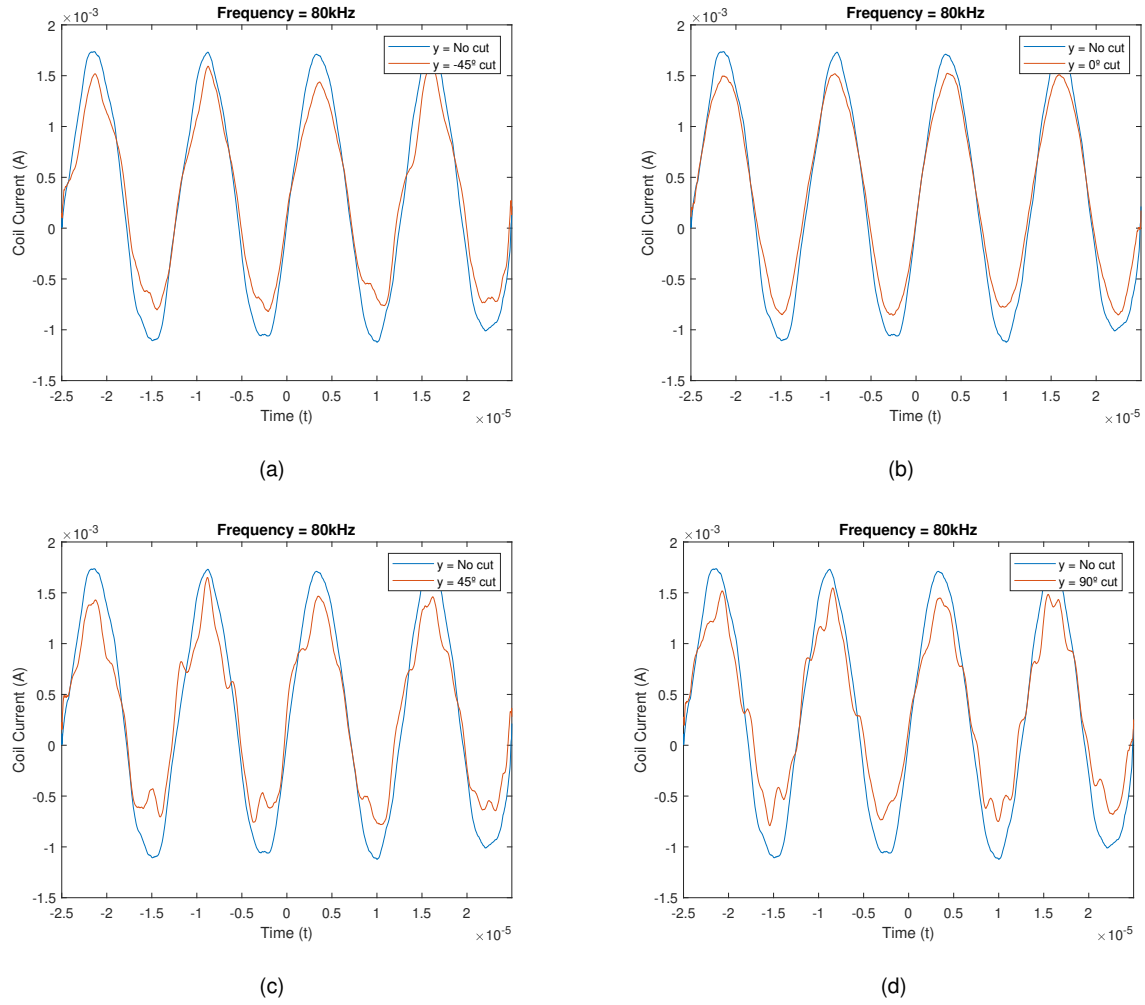

Figure 4.6: Coil current 80kHz with cuts of: (a) $-45°$; (b) $0°$; (c) $45°$; (d) $90°$.

For the 80kHz frequency, it is difficult to discern differences between each cut by visual analysis alone. However, it is possible to conclude that in terms of the results for superficial cuts, 80kHz appears to be the most promising frequency. Despite the presence of noise, it appears that there is detection in every type of cut. For a more comprehensive understanding and to confirm these results, it is essential to analyze table 4.3.

Table 4.3: Current variations

Frequency	Current variation [mA]					Current variation [%]				
	$-45°$	$0°$	$45°$	$90°$	Reference	$-45°$	$0°$	$45°$	$90°$	Reference
800Hz	0.55	0.11	0.12	0.46	0.06	12.7	2.54	2.55	10.6	1.38
8kHz	0.28	0.01	-0.058	0.12	0.06	10.6	0.37	2.19	4.48	2.25
80kHz	0.14	0.23	0.23	0.25	0.06	8.13	13.5	13.5	14.5	3.3

The 800Hz and 8kHz frequencies exhibit greater sensitivity to both the $-45°$ and $90°$ cuts. Upon closer examination of figure 3.16, it becomes apparent that variations in the quality of readings for the cuts are likely due to the utilization of non-ideal machinery. The cuts vary in length, and the distribution of broken strands is not uniform from one cut to another. It can also be inferred that the $-45°$ and $90°$ cuts encompass a greater number of broken strands within the coil range, contributing to the more significant variations observed in these cases.

The findings suggest that a frequency of approximately 80kHz is the most suitable for surface testing. While the presence of noise may hinder precise quantitative evaluation, visual inspection reveals variations across all types of cuts. Notably, at 80kHz, the sensor displays heightened sensitivity to defects. These observations offer insights into the responses of the sensor, suggesting that it may be influenced by differences in cut depths, cut angles, and the number of strands cut.

4.3.4 Flaw detection: Cuts in more than one layer of aluminum

To gain a comprehensive understanding of how the sensor's response varies with the depth of defects, an extensive analysis was conducted. This analysis encompassed a wider range of frequencies, from 8Hz to 80kHz, with the objective of investigating its capacity to detect defects across all aluminum layers within the cable. The results of this investigation are presented in figures 4.7 and 4.8.

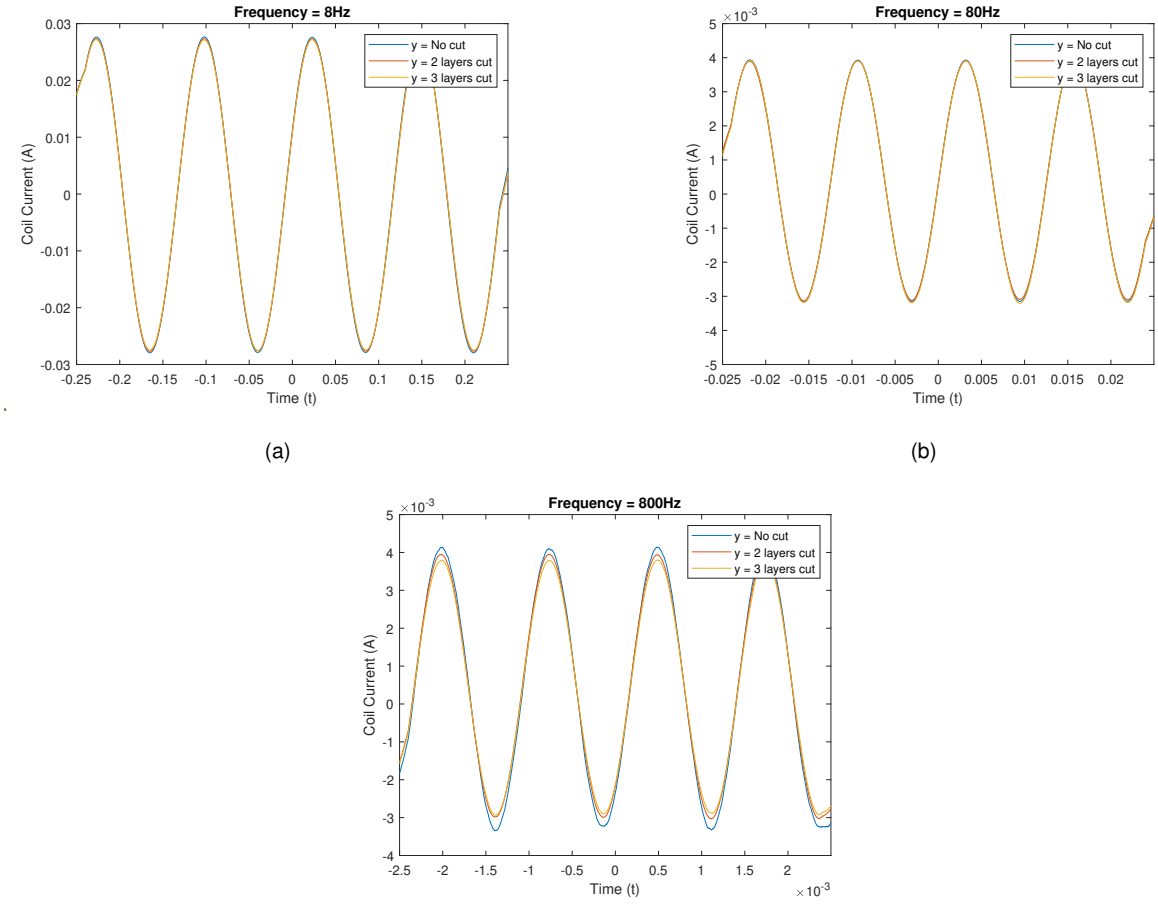

Figure 4.7: Coil current: (a) 8Hz; (b) 80Hz; (c) 800Hz.

It is evident that only the 800 Hz frequency provides significant results in this initial analysis. Moreover, differences in the responses of cables with two broken layers and three broken layers are observed.

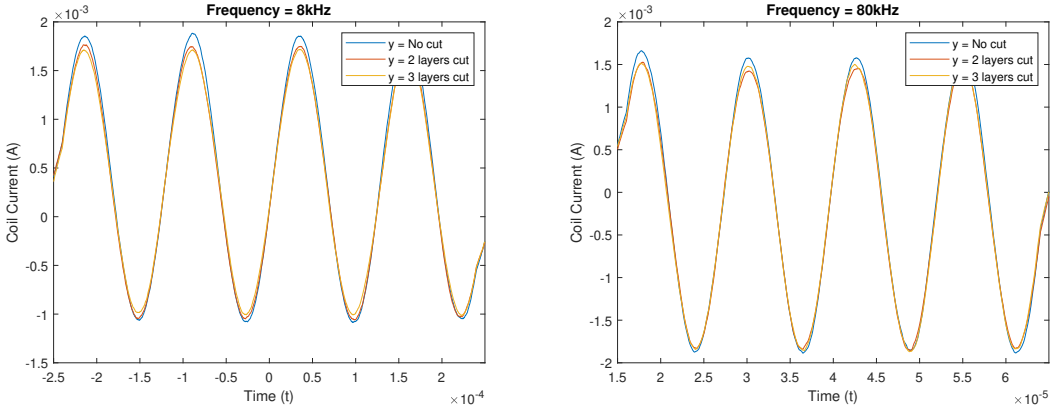

(a) (b)

Figure 4.8: Coil current: (a) 8kHz; (b) 80kHz.

At both 8kHz and 80kHz, don't seem to be any noticeable differences in the sensor's responses between the cuts with two layers and three layers.

Table 4.4: Coil current variations

Frequency	Current variation [mA]			Current variation [%]		
	2 layers	3 layers	Reference value	2 layers	3 layers	Reference value
8Hz	0.28	0.40	0.08	1.01	1.45	0.29
80Hz	0.02	0.03	0.04	0.51	0.76	1.02
800Hz	0.20	0.34	0.06	4.84	8.22	1.44
8kHz	0.12	0.14	0.03	6.50	7.56	1.41
80kHz	0.13	0.10	0.04	8.26	6.35	2.50

The data in the table confirms that the variations at 8Hz and 80Hz are not significant. This suggests that either the penetration depth is high enough to reach the uncut steel layer, or the frequencies are too low to yield significant measurements.

At 800Hz, it's clear that the eddy currents are perturbed by both depths, with more perturbation observed at the 3-layer depth. This implies that 800Hz can reach a depth of three layers.

In contrast, for both 8kHz and 80kHz, there are no significant differences between two layers and three layers. This might be because these frequencies don't permit eddy currents to penetrate deep enough to reach the third layer.

Based on these findings, we can theorize that the most suitable frequencies for detecting defects in each layer are as follows:

- 80kHz is the most effective frequency for detecting defects in the first layers, supported by its positive results in previous trials and notable sensitivity to defects in the second layer in this trial.
- 8kHz seems suitable for detecting defects in the second layer, as the variation values are clearer compared to the 80kHz values, indicating higher sensitivity to defects in this layer.
- The frequency of 800Hz emerges as the preferred choice for detecting defects in the third layer, with noticeable differences between the result of two layers and three layers cuts, and positive results for configurations involving three layers.

Chapter 5

Conclusions

Overhead line inspections are standard procedures typically performed by workers using either energized line techniques or distant visual inspection methods [30]. These transmission lines are often elevated and pose significant safety risks, complexities, and operational inefficiencies. These challenges necessitate substantial efforts to enhance live-line system safety, as disruptions can impact the power supply [31]. In light of these issues, power transmission companies are under pressure to develop innovative tools and techniques that can replace traditional manual operations [31].

Semi-autonomous robots have emerged as a potential solution to improve worker safety by enabling remote and precise inspections of conductors [32]. Therefore, the primary objective of this research is to investigate the mobility of such robots and explore the development and testing of an eddy current sensor to be integrated into these robots for inspection purposes.

To achieve these goals, we conducted trials onREN's substation in Palmela to assess the robot's mobility. These trials included evaluating the robot's performance in ascending slopes, overcoming obstacles, and maintaining stability. The robot demonstrated effective traction on slopes and could surmount obstacles, albeit with some additional assistance for stability. Additionally, a simulation was conducted to evaluate traction and speed control, showing promising results for future implementation.

On the sensor front, we conducted laboratory trials using a prototype of an eddy current sensor. The sensor was tested at frequencies ranging from 8Hz to 80kHz, initially on simple tubes composed of single materials. These trials successfully detected a significant number of defects, including cuts and corrosion on the tube's surface, with detection rates reaching approximately 10% for cuts and 12% for corrosion. Subsequent trials focused on ACSR cables and defects within the strands, such as cuts ranging from 1cm to 5cm in length, depths spanning 1 to 3 layers, and cuts affecting 2 to 5 strands. These trials yielded results consistent with the previous tests, with maximum variation rates of approximately 13%. Our conclusion is that clear detections typically correspond to variations of around 10%, while less certain detections are approximately 4% or more than double the reference value.

As a result of this research, we improved the mobility of an initial robot prototype, making it capable of traversing the entire length of the transmission lines, with the exception of the towers. The findings from the sensor trials confirmed the value of this type of sensor for integration into such robots, demonstrating

its precision in detecting defects.

It's essential to clarify that the objective of this thesis was to confirm the viability of this sensor for this application and lay the groundwork for the development of a future prototype for real-world inspection tasks. Areas for further research and future work include:

- Active Balance System: Research and development are required to address issues caused by wind and line oscillations, which affect the robot's stability and straight-line navigation. The implementation of an active balance system is essential to improve obstacle-crossing performance.

- Impedance analysis: Enhance data processing techniques for impedance analysis. This will provide more detailed information about defects, including their type, size, and depth, enabling more precise defect characterization.

- Optimization of the probe: Improve the sensor probe by implementing multiple coil configurations, including excitation and pick-up coils. This enhancement aims to increase sensitivity and accuracy in defect detection.

- Under surface tests and steel detection: Investigate methods for under-surface inspection and the detection of steel layers. Overcoming limitations in creating defects in samples will allow for a more comprehensive assessment, including control flaw size and the number of strands cut.

- Sensor Optimization: Focus on optimizing the sensor's calibration, signal processing, and noise reduction techniques to enhance its overall performance.

- Implementation of software: Develop software for control, real-time data analysis, and remote robot operation. This will improve the efficiency of inspections and provide tools for data analysis and control.

Bibliography

[1] M. Schwarz and D. Drudi. Workplace hazards facing line installers and repairers. *Monthly Lab. Rev.*, 141:1, 2018. URL https://www.bls.gov/opub/mlr/2018/article/workplace-hazards-facing-line-installers-and-repairers.htm.

[2] REN. Ren is the entity responsible for the security and continuity of the electricity service., 2023. URL https://www.ren.pt/en-gb/activity/electricity.

[3] J. da Costa Moreira. Aplicação do método rcm às linhas de muito alta tensão da ren, 09 2005. URL https://repositorio-aberto.up.pt/bitstream/10216/12339/2/Texto%20integral.pdf.

[4] C. international des grands réseaux électriques. Comité d'études b2, guide on repair of conductors and conductor-fitting systems, 2017.

[5] C. international des grands réseaux électriques. Comité d'études B2. *The Use of Robotics in Assessment and Maintenance of Overhead Lines*. CIGRÉ, 2018.

[6] N. Pouliot, P.-L. Richard, and S. Montambault. Linescout technology opens the way to robotic inspection and maintenance of high-voltage power lines. *IEEE Power and Energy Technology Systems Journal*, 2(1):1–11, 2015.

[7] P. Debenest, M. Guarnieri, K. Takita, E. F. Fukushima, S. Hirose, K. Tamura, A. Kimura, H. Kubokawa, N. Iwama, and F. Shiga. Expliner-robot for inspection of transmission lines. In *2008 IEEE International Conference on Robotics and Automation*, pages 3978–3984. IEEE, 2008.

[8] Y. Song, H. Wang, Y. Jiang, and L. Ling. Aape-d: A novel power transmission line maintenance robot for broken strand repair. In *2012 2nd International Conference on Applied Robotics for the Power Industry (CARPI)*, pages 108–113. IEEE, 2012.

[9] AM. Instructions for use traction machine with radio control, 2019.

[10] A. N. de Lucena, B. M. F. da Silva, and L. M. G. Gonçalves. Micro aerial vehicle with basic risk of operation. *Scientific Reports*, 12(1):12772, 2022.

[11] Schiebel. Schiebel demonstrates use of camcopter s-100 uas for power line patrol, 09 2013. URL https://verticalmag.com/press-releases/schiebel-demonstrates-use-of-camcopter-s-100-uas-for-power-l/.

[12] A. Snyders, J. Ferguson, J. Enslin, and P. Reichmeider. Avoiding costly plant shutdowns by employing specialized live technologies and safe practices. In *IEEE PES General Meeting*, pages 1–6. IEEE, 2010.

[13] D. Schmidt and K. Berns. Climbing robots for maintenance and inspections of vertical structures—a survey of design aspects and technologies. *Robotics and Autonomous Systems*, 61(12):1288–1305, 2013.

[14] C. Liao, Y. Yi, T. Chen, C. Cai, Z. Deng, X. Song, and C. Lv. Detecting broken strands in transmission lines based on pulsed eddy current. *Metals*, 12(6):1014, 2022.

[15] R. N. d. S. Célio Fonseca Barbosa, Flávio Eduardo Nallin. Device and method for inspecting aluminum cables with a steel core (aluminum conductor steel reinforced - ascr) installed in energized electrical energy lines, 2017.

[16] Y. I. Brahim, J. Bellemare, G. Rousseau, N. Pouliot, D. Ménard, and F. Sirois. Ultrasensitive lightweight magnetic probe for non-destructive inspection of high-voltage overhead lines. *NDT & E International*, 134:102781, 2023.

[17] N. A. Jaffrey and S. Hettiwatte. Corrosion detection in steel reinforced aluminium conductor cables. In *2014 Australasian Universities Power Engineering Conference (AUPEC)*, pages 1–6. IEEE, 2014.

[18] J. Sutton. Apparatus for an method of monitoring the corrosion in electrical power cables by measuring the variation in induced eddy currents, Mar. 24 1987. US Patent 4,652,823.

[19] C. F. Barbosa, F. E. Nallin, and R. N. De Souza. Device and method for inspecting aluminum cables with a steel core (aluminum conductor steel reinforced—ascr) installed in energized electrical energy lines, July 4 2017. US Patent 9,696,280.

[20] A. Sophian, G. Tian, D. Taylor, and J. Rudlin. Electromagnetic and eddy current ndt: a review. *Insight*, 43(5):302–306, 2001.

[21] A. N. AbdAlla, M. A. Faraj, F. Samsuri, D. Rifai, K. Ali, and Y. Al-Douri. Challenges in improving the performance of eddy current testing. *Measurement and Control*, 52(1-2):46–64, 2019.

[22] J. García-Martín, J. Gómez-Gil, and E. Vázquez-Sánchez. Non-destructive techniques based on eddy current testing. *Sensors*, 11(3):2525–2565, 2011.

[23] Nondestructive evaluation techniques : Eddy current testing. URL `https://www.nde-ed.org/NDETechniques/EddyCurrent/index.xhtml`.

[24] x engineer.org. How to calculate wheel curb climbing torque – x-engineer.org, 2022. URL `https://x-engineer.org/curb-climb-torque/`.

[25] Blickle. Wheel and castor series - choose from 30,000 products, 2023. URL `https://www.blickle.com/products/wheel-castor-series`.

[26] Filaflex tpe 82a 500g grey - recreus, 2023. URL https://evolt.pt/produto/filaflex-tpe-82a-500g-grey-recreus/.

[27] Shore a hardness scale: Definition, uses, types, benefits, and limitations, 05 2023. URL https://www.xometry.com/resources/materials/shore-a-hardness-scale/.

[28] Cabelte. Zambeze. Technical report, Cabelte, 2003.

[29] P. Yedamale. Brushless dc (bldc) motor fundamentals. *Microchip Technology Inc*, 20(1):3–15, 2003.

[30] R. A. Velásquez and J. M. Lara. Robot unit for cost and time balance using automatic inspection on overhead lines. In *2016 IEEE ANDESCON*, pages 1–4, 2016. doi: 10.1109/ANDESCON.2016.7836194.

[31] G. Rui, Z. Feng, C. Lei, and Y. Jun. A mobile robot for inspection of overhead transmission lines. In *Proceedings of the 2014 3rd International Conference on Applied Robotics for the Power Industry*, pages 1–3, 2014. doi: 10.1109/CARPI.2014.7030054.

[32] R. Miller, F. Abbasi, and J. Mohammadpour. Power line robotic device for overhead line inspection and maintenance. *Industrial Robot: An International Journal*, 44(1):75–84, 2017.

Appendix A

Technical Data Sheets

Both A.1 and A.2 were utilized to obtain crucial values for simulating the robot, as well as for decide the dimensions of the traction wheels.

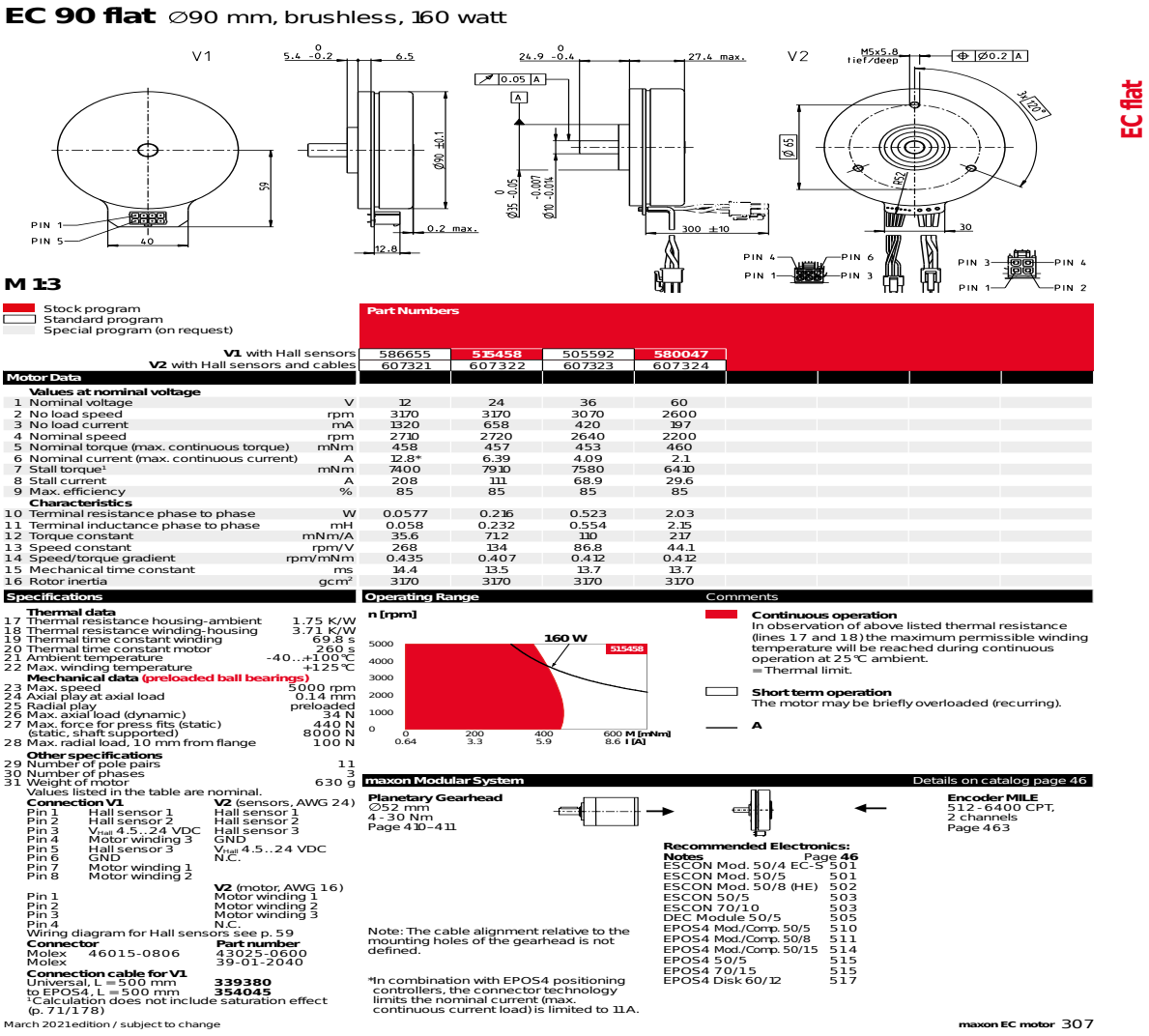

EC 90 flat ∅90 mm, brushless, 160 watt

EC flat

V1

V2

M 1:3

Stock program
Standard program
Special program (on request)

	Part Numbers			
V1 with Hall sensors	586655	515458	505592	580047
V2 with Hall sensors and cables	607321	607322	607323	607324

Motor Data					
Values at nominal voltage					
1 Nominal voltage	V	12	24	36	60
2 No load speed	rpm	3170	3170	3070	2600
3 No load current	mA	1320	658	420	197
4 Nominal speed	rpm	2710	2720	2640	2200
5 Nominal torque (max. continuous torque)	mNm	458	457	453	460
6 Nominal current (max. continuous current)	A	12.8*	6.39	4.09	2.1
7 Stall torque¹	mNm	7400	7910	7580	6410
8 Stall current	A	208	111	68.9	29.6
9 Max. efficiency	%	85	85	85	85
Characteristics					
10 Terminal resistance phase to phase	W	0.0577	0.216	0.523	2.03
11 Terminal inductance phase to phase	mH	0.058	0.232	0.554	2.15
12 Torque constant	mNm/A	35.6	71.2	110	217
13 Speed constant	rpm/V	268	134	86.8	44.1
14 Speed/torque gradient	rpm/mNm	0.435	0.407	0.412	0.412
15 Mechanical time constant	ms	14.4	13.5	13.7	13.7
16 Rotor inertia	gcm²	3170	3170	3170	3170

Specifications

Thermal data

17	Thermal resistance housing-ambient	1.75 K/W
18	Thermal resistance winding-housing	3.71 K/W
19	Thermal time constant winding	69.8 s
20	Thermal time constant motor	260 s
21	Ambient temperature	-40..+100°C
22	Max. winding temperature	+125°C

Mechanical data (preloaded ball bearings)

23	Max. speed	5000 rpm
24	Axial play at axial load	0.14 mm
25	Radial play	preloaded
26	Max. axial load (dynamic)	34 N
27	Max. force for press fits (static) (static, shaft supported)	440 N 8000 N
28	Max. radial load, 10 mm from flange	100 N

Other specifications

29	Number of pole pairs	11
30	Number of phases	3
31	Weight of motor	630 g

Values listed in the table are nominal.

Connection V1		**V2** (sensors, AWG 24)
Pin 1	Hall sensor 1	Hall sensor 1
Pin 2	Hall sensor 2	Hall sensor 2
Pin 3	V_{Hall} 4.5..24 VDC	Hall sensor 3
Pin 4	Motor winding 3	GND
Pin 5	Hall sensor 3	V_{Hall} 4.5..24 VDC
Pin 6	GND	N.C.
Pin 7	Motor winding 1	
Pin 8	Motor winding 2	

	V2 (motor, AWG 16)
Pin 1	Motor winding 1
Pin 2	Motor winding 2
Pin 3	Motor winding 3
Pin 4	N.C.

Wiring diagram for Hall sensors see p. 59

Connector	**Part number**
Molex 46015-0806	43025-0600
Molex	39-01-2040

Connection cable for V1
Universal, L = 500 mm **339380**
to EPOS4, L = 500 mm **354045**

¹Calculation does not include saturation effect (p. 71/178)

Operating Range

n [rpm]

Comments

Continuous operation
In observation of above listed thermal resistance (lines 17 and 18) the maximum permissible winding temperature will be reached during continuous operation at 25°C ambient.
= Thermal limit.

Short term operation
The motor may be briefly overloaded (recurring).

A

maxon Modular System Details on catalog page 46

Planetary Gearhead
∅52 mm
4 - 30 Nm
Page 410-411

Encoder MILE
512 - 6400 CPT,
2 channels
Page 463

Recommended Electronics:

Notes	Page **46**
ESCON Mod. 50/4 EC-S	501
ESCON Mod. 50/5	501
ESCON Mod. 50/8 (HE)	502
ESCON 50/5	503
ESCON 70/10	503
DEC Module 50/5	505
EPOS4 Mod./Comp. 50/5	510
EPOS4 Mod./Comp. 50/8	511
EPOS4 Mod./Comp. 50/15	514
EPOS4 50/5	515
EPOS4 70/15	515
EPOS4 Disk 60/12	517

Note: The cable alignment relative to the mounting holes of the gearhead is not defined.

*In combination with EPOS4 positioning controllers, the connector technology limits the nominal current (max. continuous current load) is limited to 11A.

March 2021edition / subject to change

maxon EC motor 307

Figure A.1: Motor data sheet

Planetary Gearhead GP 52 C ∅52 mm, 4.0–30.0 Nm

Ceramic Version

gear

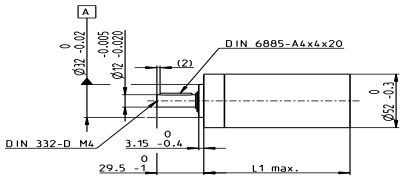

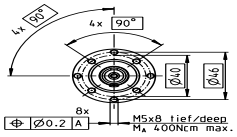

M 1:4

Technical Data					
Planetary Gearhead					straight teeth
Output shaft					stainless steel
Bearing at output					preloaded ball bearings
Radial play, 12 mm from flange					max. 0.06 mm
Axial play at axial load					0 mm
					> 5 N max. 0.3 mm
Max. axial load (dynamic)					200 N
Max. force for press fits					500 N
Direction of rotation, drive to output					=
Max. continuous input speed					6000 rpm
Recommended temperature range					-15...+80°C
Extended range as option					-40...+100°C
Number of stages	1	2	3	4	
Max. radial load, 12 mm from flange	420 N	630 N	900 N	900 N	

Stock program
Standard program
Special program (on request)

			Part Numbers						
			223080	223083	223089	223094	223097	223104	223109
Gearhead Data									
1	Reduction		3.5 :1	12 :1	43 :1	91 :1	150 :1	319 :1	546 :1
2	Absolute reduction		7/2	49/4	343/8	91	2401/16	637/2	546
10	Mass inertia	gcm²	20.7	17.6	17.3	16.7	17.3	16.8	16.4
3	Max. motor shaft diameter	mm	10	10	10	10	10	10	10
	Part Numbers		223081	223084	223090	223095	223099	223105	223110
1	Reduction		4.3 :1	15 :1	53 :1	113 :1	186 :1	353 :1	676 :1
2	Absolute reduction		13/3	91/6	637/12	338/3	4459/24	28561/81	676
10	Mass inertia	gcm²	12	16.8	17.2	9.3	17.3	9.4	9.1
3	Max. motor shaft diameter	mm	8	10	10	8	10	8	8
	Part Numbers			223085	223091	223096	223101	223106	223111
1	Reduction			19 :1	66 :1	126 :1	230 :1	394 :1	756 :1
2	Absolute reduction			169/9	1183/18	126	8281/36	1183/3	756
10	Mass inertia	gcm²		9.5	16.7	16.4	16.8	16.7	16.4
3	Max. motor shaft diameter	mm		8	10	10	10	10	10
	Part Numbers			223086	223092	223098	223102	223107	223112
1	Reduction			21 :1	74 :1	156 :1	257 :1	441 :1	936 :1
2	Absolute reduction			21	147/2	156	1029/4	441	936
10	Mass inertia	gcm²		16.5	17.2	9.1	17.3	16.5	9.1
3	Max. motor shaft diameter	mm		10	10	8	10	10	8
	Part Numbers			223087	223093		223103	223108	
1	Reduction			26 :1	81 :1		285 :1	488 :1	
2	Absolute reduction			26	2197/27		1537/54	4394/9	
10	Mass inertia	gcm²		9.1	9.4		16.7	9.4	
3	Max. motor shaft diameter	mm		8	8		10	8	
4	Number of stages		1	2	3	3	4	4	4
5	Max. continuous torque	Nm	4	15	30	30	30	30	30
6	Max. intermittent torque at gear output	Nm	6	22.5	45	45	45	45	45
7	Max. efficiency	%	91	83	75	75	68	68	68
8	Weight	g	460	620	770	770	920	920	920
9	Average backlash no load	°	0.6	0.8	1.0	1.0	1.0	1.0	1.0
11	Gearhead length L1	mm	49.0	65.0	78.5	78.5	92.0	92.0	92.0

+ Motor	Page	+ Sensor	Page	Brake	Page	Overall length [mm] = Motor length + gearhead length + (sensor/brake) + assembly parts						
RE 40, 150 W	151					120.1	136.1	149.6	149.6	163.1	163.1	163.1
RE 40, 150 W	151	MR	479			131.5	147.5	161.0	161.0	174.5	174.5	174.5
RE 40, 150 W	151	HED_5540	486/489			140.8	156.8	170.3	170.3	183.8	183.8	183.8
RE 40, 150 W	151	HEDL 9140	493			174.1	190.1	203.6	203.6	217.1	217.1	217.1
RE 40, 150 W	151			AB 28	535	156.2	172.2	185.7	185.7	199.2	199.2	199.2
RE 40, 150 W	151			AB 28	536	164.2	180.2	193.7	193.7	207.2	207.2	207.2
RE 40, 150 W	151	HED_5540	486/489	AB 28	535	173.4	189.4	202.9	202.9	216.4	216.4	216.4
RE 40, 150 W	151	HEDL 9140	493	AB 28	536	184.6	200.6	214.1	214.1	227.6	227.6	227.6
RE 50, 200 W	152					157.1	173.1	186.6	186.6	200.1	200.1	200.1
RE 50, 200 W	152	HED_5540	487/489			177.8	193.8	207.3	207.3	220.8	220.8	220.8
RE 50, 200 W	152	HEDL 9140	494			219.5	235.5	249.0	249.0	262.5	262.5	262.5
RE 50, 200 W	152			AB 44	540	219.5	235.5	249.0	249.0	262.5	262.5	262.5
RE 50, 200 W	152	HEDL 9140	494	AB 44	540	232.5	248.5	262.0	262.0	275.5	275.5	275.5
EC 40, 170 W	239					129.1	145.1	158.6	158.6	172.1	172.1	172.1
EC 40, 170 W	239	HED_5540	487/489			152.5	168.5	182.0	182.0	195.5	195.5	195.5
EC 40, 170 W	239	Res 26	496			156.3	172.3	185.8	185.8	199.3	199.3	199.3
EC 40, 170 W	239			AB 32	537	171.8	187.8	201.3	201.3	214.8	214.8	214.8
EC 40, 170 W	239	HED_5540	487/489	AB 32	537	190.2	206.2	219.7	219.7	233.2	233.2	233.2
EC 45, 150 W	240					160.3	176.3	189.8	189.8	203.3	203.3	203.3
EC 45, 150 W	240	HEDL 9140	493			175.9	191.9	205.4	205.4	218.9	218.9	218.9
EC 45, 150 W	240	Res 26	496			160.3	176.3	189.8	189.8	203.3	203.3	203.3
EC 45, 150 W	240			AB 28	536	167.7	183.7	197.2	197.2	210.7	210.7	210.7
EC 45, 150 W	240	HEDL 9140	493	AB 28	536	184.7	200.7	214.2	214.2	227.7	227.7	227.7
EC 45, 250 W	241					193.1	209.1	222.6	222.6	236.1	236.1	236.1
EC 45, 250 W	241	HEDL 9140	493			208.7	224.7	238.2	238.2	251.7	251.7	251.7
EC 45, 250 W	241	Res 26	496			193.1	209.1	222.6	222.6	236.1	236.1	236.1

March 2021 edition / subject to change

Figure A.2: Gearbox data sheet